Monthly Notices of the ROYAL ASTRONOMICAL SOCIETY

MNRAS **518,** 5414–5443 (2023) https://doi.org/10.1093/mnras/stac3378
Advance Access publication 2022 November 21

High-resolution spectroscopic analysis of four new chemically peculiar stars

M. P. Roriz [1]★ C. B. Pereira,[1] S. Junqueira,[1] M. Lugaro,[2,3,4] N. A. Drake[1,5,6] and C. Sneden[7]

[1]*Observatório Nacional/MCTI, Rua Gen. José Cristino, 77, 20921-400 Rio de Janeiro, Brazil*
[2]*Konkoly Observatory, Research Centre for Astronomy and Earth Sciences, Eötvös Loránd Research Network (ELKH), H-1121 Budapest, Konkoly Thege M. út 15-17, Hungary*
[3]*Institute of Physics, ELTE Eötvös Loránd University, H-1117 Budapest, Pázmány Péter sétány 1/A, Hungary*
[4]*School of Physics and Astronomy, Monash University, VIC 3800, Australia*
[5]*Laboratory of Observational Astrophysics, Saint Petersburg State University, Universitetski pr. 28, 198504 Saint Petersburg, Russia*
[6]*Laboratório Nacional de Astrofísica/MCTI, Rua dos Estados Unidos 154, Bairro das Nações, 37504-364 Itajubá, Brazil*
[7]*Department of Astronomy and McDonald Observatory, The University of Texas, Austin, TX 78712, USA*

Accepted 2022 November 11. Received 2022 November 11; in original form 2022 May 12

ABSTRACT

We present detailed chemical compositions of four stars on the first-ascent red giant branch that are classified as chemically peculiar, but lack comprehensive analyses at high spectral resolution. For BD+03°2688, HE 0457−1805, HE 1255−2324, and HE 2207−1746, we derived metallicities [Fe/H] = −1.21, −0.19, −0.31, and −0.55, respectively, indicating a range in Galactic population membership. In addition to atmospheric parameters, we extracted elemental abundances for 28 elements, including the evolutionary-sensitive CNO group and $^{12}C/^{13}C$ ratios. Novel results are also presented for the heavy elements tungsten and thallium. All four stars have very large enhancements of neutron-capture elements, with high [La/Eu] ratios indicating enrichments from the *slow* neutron capture (*s*-process). To interpret these abundances, all indicative of [*s*/Fe] >1.0, we compared our results with data from literature, as well as with predictions from the Monash and FRUITY *s*-process nucleosynthesis models. BD+03°2688, HE 1255−2324, and HE 2207−1746 show C/O >1, while HE 0457−1805 has C/O <1. Since HE 0457−1805 and HE 1255−2324 are binary stars, their peculiarities are attributable to mass transfer. We identified HE 0457−1805 as a new barium giant star, and HE 1255−2324 as a new CH star, in fact a higher metallicity analogue CEMP-*r*/*s* star; the single object reported in literature so far with similar characteristics is the barium star HD 100503 ([Fe/H] = −0.72). A systematic monitoring is needed to confirm the binary nature of BD+03°2688 and HE 2207−1746, which are probably CH stars.

Key words: nuclear reactions, nucleosynthesis, abundances – stars: abundances – stars: AGB and post-AGB – stars: chemically peculiar – stars: evolution – stars: fundamental parameters.

1 INTRODUCTION

The chemical abundance profiles of stellar atmospheres, revealed from their observed spectra, give us strong constraints on the environments where the stars were formed as well as their subsequent evolution. Chemically peculiar stars, in particular, are objects whose abundance distributions differ from those observed in normal stars of the same age and Galactic field population. Many of these chemical peculiarities can be interpreted in the light of the mass transfer hypothesis between the components of a binary systems or even as consequence of a previous enrichment of the natal cloud. Such characteristics make these stars important targets for investigation. To disentangle the possible events able to produce these peculiarities, detailed chemical abundance studies are needed as they provide valuable data set for testing and constraining theoretical nucleosynthesis models, as well as the feasible astrophysical sources. Barium stars (Bidelman & Keenan 1951), CH stars (Keenan 1942), and the carbon-enhanced metal-poor (CEMP) stars (Beers & Christlieb 2005), among others, are examples of different classes of chemically peculiar objects, each displaying its own characteristics.

Barium stars and CH stars exhibit atmospheres rich in both carbon and elements created by the *slow* neutron-capture process (the *s*-process; Käppeler et al. 2011). The *s*-process takes place within the deep layers of evolved stars, when they reach the asymptotic giant branch (AGB; Karakas & Lattanzio 2014) stage of the stellar evolution. During their thermally pulsing (TP-AGB) phase, the stars self-enrich their atmospheres through the convective mixing episodes known as third dredge-up (TDU), which bring the by-products of nucleosynthesis to their external layers. However, since barium stars and CH stars are not luminous enough objects to be considered TP-AGB stars, they were not able to internally synthesize heavy elements observed on their atmospheres.

In fact, the characteristic overabundance of *s*-elements, as easily seen in the very strong *n*-capture transitions such as the Ba II and Sr II lines in barium and CH stars, as well as their anomalously deep molecular CH, CN, and C_2 bands, are understood in the light of the mass transfer mechanism between the components of a binary

★ E-mail: michelle@on.br

system; their chemical peculiarities are from extrinsic origin. In this picture, the primary evolved star, now an invisible white dwarf, transferred the material previously processed in its AGB phase to the secondary star, now observed as a barium star or CH star. Indeed, since the 1980s, this astrophysical scenario has been confirmed (McClure, Fletcher & Nemec 1980; McClure 1984; McClure & Woodsworth 1990) and extended (e.g. Jorissen et al. 1998, 2019) from data of the radial velocity monitoring programs that show orbital motion for these objects. Thus, the chemical abundance pattern recorded in the atmospheres of CH stars and barium stars provides us with clues from which we can probe and infer about the physical conditions inside the former AGB companion star.

Although the same astrophysical scenario is invoked to explain the origins of CH stars and barium stars, these objects have individual spectroscopic characteristics that warrant closer attention. CH stars are the Population II analogues of barium stars. While CH stars are metal-poor objects, belonging to the halo population, showing high radial velocities, barium stars are objects commonly associated with the disc of the Galaxy. CH stars exhibit C/O >1, whereas barium stars exhibit C/O <1. Several studies have provided elemental abundances of different chemical elements for barium stars (e.g. Barbuy et al. 1992; Allen & Barbuy 2006; Pereira et al. 2011; de Castro et al. 2016; Karinkuzhi et al. 2018; Shejeelammal et al. 2020; Roriz et al. 2021a, b) and CH stars (e.g. Vanture 1992b, c; Goswami 2005; Pereira & Drake 2009; Pereira et al. 2012; Karinkuzhi & Goswami 2014; Goswami, Aoki & Karinkuzhi 2016; Purandardas et al. 2019). As far as the enrichment levels of the *s*-process elements are concerned, the atmospheres of CH stars are more *s*-rich than the atmospheres of barium stars; in fact, this is a typical feature of the *s*-process in low-metallicities, where seed nuclei experience higher neutron exposures. In general, barium stars have orbital periods longer than those commonly observed in CH stars, and display more eccentric orbits than CH stars. Taken together, the abundance patterns and the orbital elements observed in these systems are used to probe the binary evolution of barium stars and CH stars, in order to constrain the mass transfer mechanism. This is a debated topic in literature, with Roche lobe overflow and wind accretion as the main channels of mass transfer to account the observations (e.g. Han et al. 1995; Jorissen et al. 1998, 2016). Therefore, studies focused on these peculiar systems are important to improve our understanding of both nucleosynthesis and the physics of mass transfer.

CEMP stars, in turn, are objects found in lower metallicity regimes ([Fe/H] <-2.0). They exhibit high carbon excess ([C/Fe] $>+1.0$) in their atmospheres, although the limit for the carbon-to-iron ratio is not strictly defined in literature. In addition to their carbon-rich nature, CEMP stars can also exhibit a high content of heavy elements ($Z > 30$), which are mainly synthesized by the *s*-process and the *rapid* neutron-capture mechanism (the *r*-process). To emphasize these characteristics, CEMP stars are labelled as CEMP-*s* and CEMP-*r*, respectively. In contrast, the CEMP-no stars do not exhibit *n*-enhancements on their surface. The so called CEMP-*r*/*s* stars are more puzzling objects, since their atmospheres are simultaneously enriched in *r*- and *s*-elements. However, as demonstrated by Hampel et al. (2016), the *intermediate* neutron-capture process (the *i*-process; Cowan & Rose 1977) is able to reproduce the chemical patterns observed in these systems. None the less, it is worth noting that there are also interesting objects displaying features of CEMP-*r*/*s*, but without carbon enhancement (Roederer et al. 2016), or with abundance profiles that are not interpreted in the light of a single/simple *i*-process (Koch et al. 2019). In fact, these classifications are based from abundance data of different chemical elements, such as Ba, La, Sr, and Eu (see e.g. Beers & Christlieb 2005; Aoki et al. 2007; Masseron et al. 2010; Spite et al. 2013; Hansen et al. 2019). Some astrophysical scenarios are proposed and debated in literature to explain the origins of the peculiarities observed in CEMP stars (see e.g. Goswami, Rathour & Goswami 2021, and their references). However, the same formation scenario of the barium stars and CH stars (i.e. mass transfer) is also invoked to explain the origin of the CEMP-*s* stars, considered as the metal-poor counterparts of the CH stars. Indeed, Lucatello et al. (2005) reported a binary frequency of $\sim$ 68 per cent in their sample of CEMP-*s*. The high binary frequency among the CEMP-*s* stars is also confirmed in further studies (e.g. Starkenburg et al. 2014; Hansen et al. 2016), which, from extensive radial velocity monitoring, corroborate that most, if not all, CEMP-*s* stars are members of binary systems.

In this study, we report a high-resolution optical spectroscopy analysis for four red giants that have been classified as either barium stars or CH stars, but have not yet been subjected to comprehensive chemical composition analyses: BD+03°2688, HE 0457−1805, HE 1255−2324, and HE 2207−1746. The star BD+03°2688 was first recognized as a chemically peculiar star by Luck & Bond (1991), who included this object into a small group of four stars as broadly labelled as 'metal-deficient barium stars' (BD+03°2688, BD+04°2466, HD 55496, and HD 104340). These authors noticed that the stars belonging to this group exhibit strong CH and C_2 molecular bands, as well as weak metallic lines; therefore, they could be the Population II analogues of the classical barium stars and probably CH candidate stars. Although these classifications were interesting and deserved further investigation at that time, the relatively low resolution ($\sim$0.2 Å) of Luck & Bond's spectra precluded deeper insights into the true nature of these stars. Given this, we decided to re-investigate and revise the meaning of 'metal-deficient barium stars', using a new high-resolution optical CCD spectra.

In fact, the stars HD 55496 and HD 104340 could not be classified as CH candidate stars due to weakness of C_2 bands. As seen by Junqueira & Pereira (2001), and later by Jorissen et al. (2005) and Drake & Pereira (2008), HD 104340 is probably a metal-poor AGB candidate star. Another example is the star HD 55496, which was considered as a field star that may have escaped from a globular cluster (Pereira et al. 2019a). The other two stars of the Luck & Bond (1991)'s group, BD+04°2466 (Pereira & Drake 2009) and BD+03°2688 (this work), in fact, exhibit strong CH and C_2 molecular bands, along with weak metallic lines, and could be strong CH candidate stars. BD+04°2466 is a CH star, since it displays the typical characteristics of the stars belonging to this class, *s*-process and carbon enrichment (Pereira & Drake 2009), and it is a binary system (Jorissen et al. 2005). BD+03°2688 is the last object of the Luck & Bond's group not yet investigated with better spectroscopy data; we included it also in our investigation.

Along with BD+03°2688, we have also added as targets the stars HE 0457−1805, HE 1255−2324, and HE 2207−1746, from the objective prism plates of the Hamburg/ESO Survey (Christlieb et al. 2001). The stars HE 0457−1805 and HE 2207−1746 came to our attention because they were previously classified as chemically peculiar stars by Goswami (2005), i.e. stars with prominent C_2 bands having, respectively, a 'HD 26' and a 'HD 209061' type spectra, both well known CH stars. HE 1255−2324 was discovered in the objective prism plates of the Hamburg/ESO Survey carbon stars (Christlieb et al. 2001). In their list, HE 1255−2324 presents low values for the band indexes $I(C_2\ \lambda4737\ Å)$ and $I(C_2\ \lambda5165\ Å)$, thus probably indicating not being a cool carbon star, where the spectrum is crowded due to the strong molecular line opacities.

The paper is organized in the following way. In Section 2, we briefly describe the setup instrumentation for the data acquisition;

Table 1. Log of the observations for the target stars analysed in this work. Column 1 gives the name of the star, column 2 gives the dates of observation, column 3 gives the S/N ratio around 6000 Å, and the last column gives the observed heliocentric radial velocity (RV) derived from Doppler shifts based on 10 absorption lines.

Star	Date of observation	S/N (at 6000 Å)	Exp. (s)	RV ($km\,s^{-1}$)
BD+03°2688	2007 Apr. 4	180	2400	32.64 ± 0.29
	2016 Mar. 18	120	1500	34.36 ± 0.19
HE 0457−1805	2007 Oct. 15	100	2×3600	61.22 ± 0.34
HE 1255−2324	2010 May 4	100	1800	37.25 ± 0.26
	2010 Aug. 1	110	1800	18.21 ± 0.21
HE 2207−1746	2007 Sep. 7	100	2×3600	-8.01 ± 0.21

in Section 3, we present the adopted methodology to derive the atmospheric parameters of the target stars; in Section 4, we describe the techniques used to obtain the chemical abundances. The results and discussion are presented in Section 5. Finally, in Section 6, we drawn the main conclusions of this study.

2 OBSERVATIONS

The high-resolution spectra of the stars analysed in this work were obtained with the Fiberfed Extended Range Optical Spectrograph (FEROS; Kaufer et al. 1999) at the 2.2 m ESO telescope in La Silla (Chile). The wavelength range obtained with FEROS covers the spectral region between 3900 and 9200 Å. The resolving power of FEROS is approximately 48 000 with a degradation less than 10 per cent over the whole wavelength range (Kaufer & Pasquini 1998). The spectra were reduced following the standard procedure, including bias subtraction, flat-fielding, order extraction, and wavelength calibration following the FEROS Data Reduction Software pipeline based on ESO-MIDAS environment. The spectra were later normalized and shifted to rest wavelengths in the regions of interest for spectral synthesis. Table 1 provides an observing log of the spectroscopic observations.

3 ATMOSPHERIC PARAMETERS

The atmospheric parameters of BD+03°2688, HE 0457−1805, HE 1255−2324, and HE 2207−1746 were determined in the same way as in the previous studies done for the stars HD 104340 and HD 206983 (Drake & Pereira 2008), the CEMP-*s* star CD−50°776 (Roriz et al. 2017), and the star HD 55496 (Pereira, Drake & Roig 2019b). We first measured the equivalent widths W/λ of the Fe I and Fe II absorption lines by fitting Gaussian profiles to the observed spectral lines. The atomic parameters, excitation potential (χ), and log *gf* values for the Fe I and Fe II lines were taken from Lambert et al. (1996). The equivalent widths of the measured Fe I and Fe II lines are shown in Table A1, presented in Appendix A; we used the task *splot* of IRAF to measure the equivalent widths.

These absorption lines were used to obtain the stellar atmospheric parameters, which are the effective temperature, $T_{\rm eff}$, the surface gravity, $\log g$, the microturbulent velocity, ξ, and the metallicity, [Fe/H].[1] In order to determine the best atmospheric model that describes the physical conditions of the stellar atmosphere of BD+03°2688, HE 0457−1805, HE 1255−2324, and HE 2207−1746, we have used the version 2013 of the spectral line analysis code MOOG[2] (Sneden 1973), which assumes the conditions of local thermodynamic equilibrium (LTE), and the 1D plane-parallel model atmospheres provided by Kurucz (1993).

The effective temperature and the microturbulent velocity are determined when, for a given atmopsheric model, there are no trends for Fe I lines between iron abundance and both excitation potential and reduced equivalent width (W_λ/λ). The surface gravity is obtained by means of the ionization equilibrium, that is, when the abundances of Fe I and Fe II are equal at the selected effective temperature. The final Fe I abundance defines the metallicity of the star. Our derived adopted atmospheric parameters for each star are given in Table 2, along with values from previous studies. The final metallicity was normalized to the iron abundance given by Grevesse & Sauval (1998), which is 7.50 dex.

Comparing the log *gf* values of the Fe II lines between the ones we used from Lambert et al. (1996) with those given by Meléndez & Barbuy (2009), we found a mean difference of −0.025 ($\sigma = 0.03$) for 11 lines in common. Therefore, there will not be a significant impact in our derived stellar parameters. In table 7 of Meléndez & Barbuy, it can be seen that the mean difference by using the log *gf* values from Lambert et al. and those of Meléndez & Barbuy is −0.01 ($\sigma = 0.07$).

A very low value of the surface gravity ($\log g = 0.0$) for BD+03°2688 was determined by Luck & Bond (1991), while we have derived $\log g = 1.6$. For this star, Luck & Bond used a photographic image-tube spectrogram with a dispersion of 4.6 Å/mm and a relatively low resolution of ∼0.2 Å (3800–5200 Å). This may explain the low gravity and the high microturbulent velocity (2.7 $km\,s^{-1}$) found by these authors. This high value for the microturbulent velocity, derived by means of neutral lines, might in turn result in the low value for $\log g$, derived by forcing the Fe II and Fe I lines to yield the same iron abundance.

For the stars HE 0457−1805, HE 1255−2324, and HE 2207−1746, previous atmospheric parameters (Table 2) were obtained by Kennedy et al. (2011), who used a different technique from that used in this work. These authors first obtained photometric temperatures, and by considering that all the stars analysed in their work were low metallicity stars (down to [Fe/H] = −1.7), they obtained the surface gravities using evolutionary tracks for that metallicities. Our derived metallicities for these stars are more than an order of magnitude higher.

The errors in temperature and microturbulent velocity were estimated considering the uncertainty in the value of the slope of the null trend, respectively, between the iron abundance given by the Fe I lines and the excitation potential, and between the iron abundance and

[1]Throughout this study, we have used the standard spectroscopy notation, $[A/B] = \log(N_A/N_B)_\star - \log(N_A/N_B)_\odot$, for two generic elements A and B.

[2]MOOG is available at: https://www.as.utexas.edu/~chris/moog.html.

Table 2. Atmospheric parameters obtained in this work for the program stars, as well as values from other studies available in literature.

Parameter	BD+03°2688 Value	Ref.	HE 0457−1805 Value	Ref.	HE 1255−2324 Value	Ref.	HE 2207−1746 Value	Ref.
$T_{\rm eff}$ (K)	4 600 ± 40	1	4 720 ± 100	1	4 960 ± 110	1	4 780 ± 80	1
	4 747 ± 46	2	4 484	4	4 405	4	4 737	4
	4 300	3	4 580	5	4 760	5		
			4 437	6	4 486	6		
					4 487	7	4 577	7
					4 530	8		
log g (dex)	1.6 ± 0.3	1	2.2 ± 0.4	1	3.0 ± 0.3	1	2.6 ± 0.3	1
	1.43 ± 0.14	2	0.77	4	0.69	4	1.23	4
	0.00	3	1.58	6	1.73	6		
					1.73	7		
					2.63	8		
[Fe/H] (dex)	−1.21 ± 0.13	1	−0.19 ± 0.17	1	−0.31 ± 0.16	1	−0.55 ± 0.15	1
	−1.27 ± 0.07	2	−1.46	4	−1.47	4	−1.87	4
	−1.42	3	+0.33	6	+0.32	6		
					+0.20	7		
ξ (km s^{-1})	1.5 ± 0.2	1	1.3 ± 0.2	1	1.5 ± 0.2	1	1.4 ± 0.2	1
	2.7	3						

Note. *References:* (1) This work; (2) Arentsen et al. (2019); (3) Luck & Bond (1991); (4) Kennedy et al. (2011); (5) Munari et al. (2014); (6) Kunder et al. (2017); (7) Stevens, Stassun & Gaudi (2017); (8) McDonald, Zijlstra & Watson (2017).

the reduced equivalent width. For the gravity, the error is estimated as the difference between the nominal value given by the ionization equilibrium and the value of log g that produces a difference between the mean abundances of Fe I and Fe II, that is equal to (or greater than) the standard deviation of the mean [Fe I/H]. The uncertainties of the obtained atmospheric parameters are also provided in Table 2.

4 ABUNDANCE ANALYSIS

We have determined abundances for several chemical elements, including light elements (C, N, O, Na, Mg, Al, Si, Ca, and Ti), iron-group elements (Cr and Ni), and neutron-capture elements (Rb, Sr, Y, Zr, Nb, Mo, Ru, La, Ce, Nd, Sm, Eu, Er, W, Tl, and Pb), either by matching predicted and measured equivalent widths or computing synthetic spectra and comparing them with the observed spectra. The elemental abundances derived in this work were also obtained from the code MOOG (Sneden 1973).

The abundances of carbon, nitrogen, oxygen, and the ^{12}C/^{13}C isotopic ratio were determined exclusively with spectral syntheses. The carbon abundance was obtained using the C_2 (0,1) band head of the system $A^3\Pi_g - X^3\Pi_u$ at 5635 Å, while the nitrogen abundance was obtained based on the ^{12}CN lines $A^2\Pi - X^2\Sigma$ in the 7994–8020 Å wavelength range. To obtain the ^{12}C/^{13}C isotopic ratio, we used the ^{13}CN lines around the region at 8004–8005 Å. Details about the molecular constants and dissociation energies of the molecules involved in the determination of the carbon and nitrogen abundances are given in Drake & Pereira (2008). The observed and synthetic spectra for the spectral regions of the C_2 molecular band, the CN molecular lines used for nitrogen abundance and the ^{13}C lines used for the determination of the ^{12}C/^{13}C isotopic ratio are shown in Figs B1, B2, and B3, provided in Appendix B. For oxygen, we determined its abundance based on the forbidden line at 6300.3 Å.

The abundances of rubidium, niobium, and europium were also determined by means of the spectral synthesis technique. Details of the spectral regions and lines used for the abundance determination are given in Roriz et al. (2021a, b). Fig. 1 shows spectral synthesis

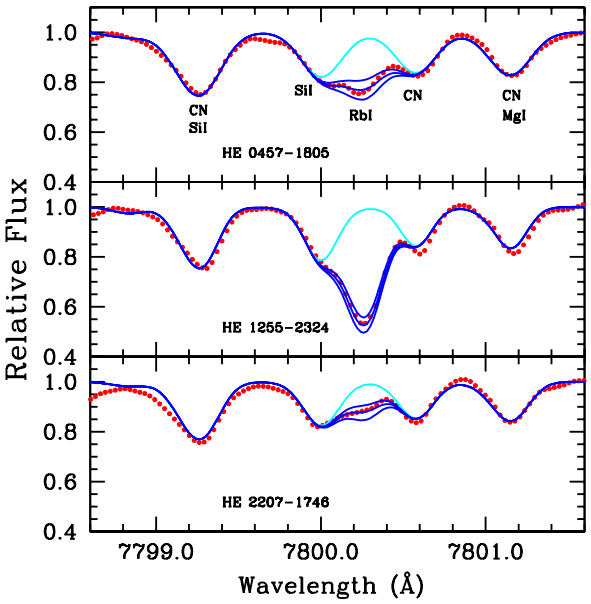

Figure 1. Observed (red dots) and synthetic (curves) spectra close to the region of the Rb I line at 7800.20 Å for the stars HE 0457−1805, HE 1255−2324, and HE 2207−1746. The upper cyan curves shown in the panels are synthetic spectra calculated without contribution from the rubidium line. The middle blue curves are synthetic spectra calculated for the adopted solutions, log ϵ(Rb) = 2.85, 3.90, and 2.45 dex, that provide the best fits for HE 0457−1805, HE 1255−2324, and HE 2207−1746, respectively; the upper and lower blue curves show the spectral synthesis for Δlog ϵ(Rb) = ±0.14 dex around the adopted solutions.

for the element rubidium around the resonant Rb I line at 7800.2 Å. However, we were not able to derive the rubidium content for the star BD+03°2688; for this star, the Rb line was too weak to be detected in its spectrum. The lead abundance was derived from the Pb I line at λ 4057.81 Å, where the isotopic shifts and hyperfine

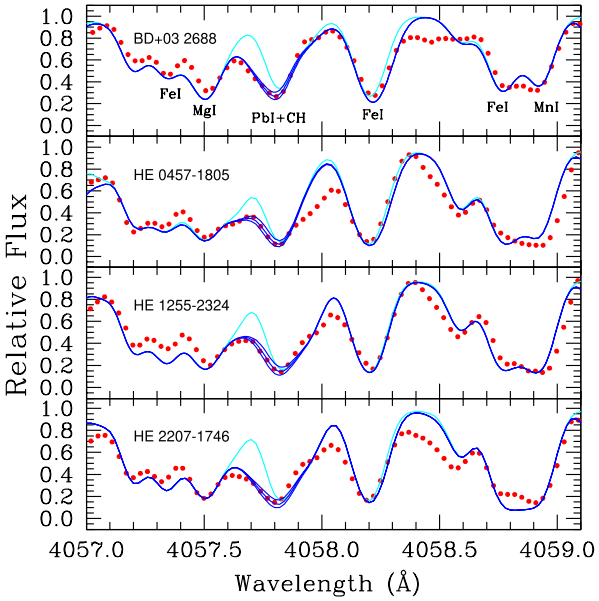

Figure 2. Observed (red dots) and synthetic (curves) spectra close to the region of the Pb I line at 4057.8 Å for the stars BD+03°2688, HE 0457−1805, HE 1255−2324, and HE 2207−1746. The upper cyan curves shown in the panels are synthetic spectra calculated without contribution from the CH lines. The middle blue curves are synthetic spectra calculated for the adopted solutions, $\log\epsilon$(Pb) = 2.25, 3.25, 3.05, and 2.95 dex, that provide the best fits for BD+03°2688, HE 0457−1805, HE 1255−2324, and HE 2207−1746, respectively; the upper and lower blue curves show the spectral synthesis for $\Delta\log\epsilon$(Pb) = ±0.20 dex around the adopted solutions.

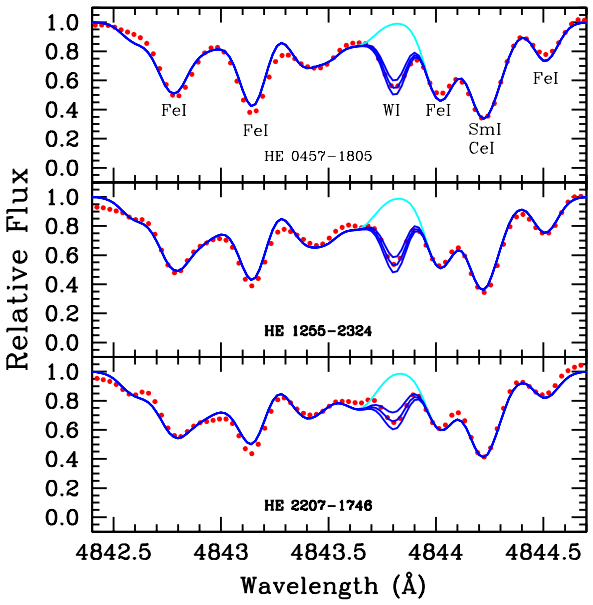

Figure 3. Observed (red dots) and synthetic (curves) spectra close to the region of the W I line at 4843.81 Å for the stars HE 0457−1805, HE 1255−2324, and HE 2207−1746. The upper cyan curves shown in the panels are synthetic spectra calculated without contribution from the tungsten line. The middle blue curves are synthetic spectra calculated for the adopted solutions, $\log\epsilon$(W) = 2.31, 2.71, and 2.01 dex, that provide the best fits for HE 0457−1805, HE 1255−2324, and HE 2207−1746, respectively; the upper and lower blue curves show the spectral synthesis for $\Delta\log\epsilon$(W) = ±0.18 dex around the adopted solutions.

splitting (HFS) were taken from Van Eck et al. (2003). In Fig. 2, we show the observed and synthetic spectra for the region around the lead line at 4057.81 Å. As one can see in Fig. 2, the CH transitions may contribute to the region where the lead line was used for the spectral synthesis. We considered the previous carbon abundance determination when we synthesized the profile at 4057.81 Å, as it was done in Roriz et al. (2017).

For the other chemical elements considered in this study, we list in Table A2 the lines used to obtain their abundances along with their excitation potentials, log *gf* values, their respective references, and the equivalent width measurements. For lanthanum, in particular, we used the same technique as employed by Roriz et al. (2021b); we measured the equivalent widths and run the driver *blends* of MOOG, which provides abundances from blended spectral lines, since the atomic terms of lanthanum are strongly affected by HFS.

We have also determined abundances of three other heavy elements not investigated before in the spectra of barium stars: erbium (Z = 68), tungsten (Z = 74), and thallium (Z = 81). The erbium absorption lines used in the abundance analysis are given in Table A2. The tungsten abundances were obtained using spectral synthesis technique of two W I lines, one at 4843.81 Å, with log gf = −1.50, and the other line at 5224.66 Å, with log gf = −1.70. The log gf values were taken from Vienna Atomic Line Database (VALD; Ryabchikova et al. 2015). Fig. 3 shows the spectral synthesis for tungsten around the line at 4843.81 Å.

To determine thallium abundances, we also used the spectral synthesis technique. We have taken into account the HFS of the atomic terms $6p\ ^2P_{3/2}$ and $7s\ ^2S_{1/2}$ involved in the transition at 5350.46 Å, for the two stable isotopes of thallium, ^{203}Tl (29.5 per cent) and ^{205}Tl (70.5 per cent), which have the same nuclear spin, I = 1/2. The adopted HFS constants, as well as the isotopic shift, were taken from Lambert, Mallia & Smith (1972), and the energy levels are provided by the National Institute of Standards and Technology (NIST; Kramida et al. 2021) data base. Thus, we were able to compute the log gf of each hyperfine component by distributing the total log gf according to the relative intensities. In this procedure, we have adopted log gf = −0.21, also provided by the NIST data base. In fact, our results are similar to that given by Wahlgren et al. (2000). We summarize in Table 3 the list of the atomic lines used to derive abundances via

Table 3. Atomic lines used to obtain the abundance by spectral synthesis. In the last column, we provide the references for log gf and HFS data.

Element	Wavelength (Å)	χ (eV)	log gf	Ref.
O I	6300.3	0.00	−9.72	1
Rb I	7800.268	0.000	+0.137	2, 3
Nb I	4606.756	0.348	−0.377	2, 4
Nb I	5344.158	0.348	−0.730	2, 4
Nb I	5350.722	0.267	−0.910	2, 4
Eu I	6645.100	1.379	+0.120	5
W I	4843.810	0.412	−1.500	2
W I	5224.660	0.599	−1.700	2
Tl I	5350.423	0.965	−1.651	6, 7
	5350.428		−0.952	
	5350.541		−1.350	
	5350.406		−1.273	
	5350.411		−0.574	
	5350.523		−0.972	
Pb I	4057.810	1.320	−0.220	8

Note. *References:* (1) Allende Prieto, Lambert & Asplund (2001) (2) VALD; (3) Roriz et al. (2021a); (4) Roriz et al. (2021b); (5) Lawler et al. (2001b); (6) NIST; (7) This work; (8) Van Eck et al. (2003).

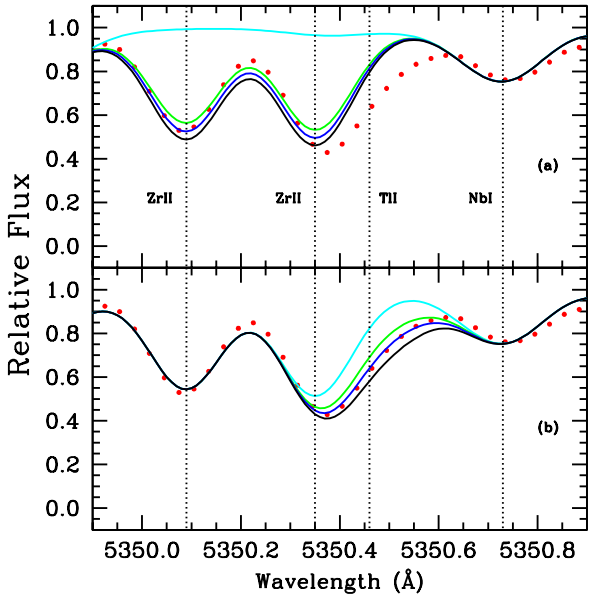

Figure 4. Observed (red dots) and synthetic (curves) spectra close to the region of the Tl I line at 5350.46 Å for the star HE 1255−2324. Vertical dotted lines represent the observed transitions due to Zr II at 5350.09 Å, Zr II at 5350.35 Å, Tl I at 5350.46 Å, and Nb II at 5350.72 Å. In panel (a), we show synthetic spectra calculated for different zirconium abundances, and without contribution from the thallium line. The upper cyan curve shows the synthesis without contribution from the zirconium line. In blue, we show the best fit based on the Zr II line at 5350.09 Å, obtained for $\log\epsilon(\mathrm{Zr}) = 4.33$ dex ([Zr/Fe] $= +2.04$). Green and black curves are synthetic spectra calculated for $\Delta\log\epsilon(\mathrm{Zr}) \pm 0.20$ dex. In panel (b), we show synthetic spectra calculated for different thallium abundances, considering the best fit for the zirconium abundance seen in panel (a). The upper cyan curve shows the synthesis without contribution from the thallium line. In blue, we show the best fit based on the Tl I line at 5350.46 Å, obtained for $\log\epsilon(\mathrm{Tl}) = 2.35$ dex ([Tl/Fe] $= +1.76$). In order to fit the whole line profile of the Zr II at 5350.35 Å, we need to add the thallium contribution in the red wing of the zirconium line. Green and black curves are synthetic spectra calculated for $\Delta\log\epsilon(\mathrm{Tl}) \pm 0.20$ dex.

spectral synthesis technique, where we provide the references for log *gf* and HFS. In particular, for thallium, we have shown in Table 3 the HFS components of the 5350.46 Å line along with the respective log *gf* values also derived in this work.

In Fig. 4, we show the thallium line at 5350.46 Å, for HE 1255−2324, where red dots represent the observed spectrum. The thallium transition lies at the red wing of the Zr II at 5350.35 Å. In Fig. 4 (a), we show that only considering the Zr II transition, assuming the same abundance of its neighbour Zr II line at 5350.09 Å, it is not possible to reproduce the observed line profile (blue curve synthesis). Higher zirconium abundance does not also fit the profile (black line synthesis). In Fig. 4 (b), we show that we were able to synthesize and reproduce to whole profile assuming a thallium abundance of $\log\epsilon(\mathrm{Tl}) = 2.35$ dex (blue curve synthesis). By doing the same analysis for HE 0457−1805 and HE 2207−1746, we obtained a thallium abundance, respectively of $\log\epsilon(\mathrm{Tl}) = 1.80$ and 1.90 dex.

Finally, Tables 4 and 5 provide the obtained abundances, their standard deviation, and the number of lines used for each species. The final abundances were normalized to the solar photospheric abundances given by Grevesse & Sauval (1998).

4.1 Abundance uncertainties

The uncertainties in abundances come from errors associated with the (i) stellar atmospheric parameters ($T_{\rm eff}$, $\log g$, ξ, and [Fe/H]) and (ii) line-to-line scatter, associated with line parameters, as equivalent width (W_λ) measurements, line blending, continuum normalization, and oscillator strength. The uncertainties due to errors in the equivalent width measurements were calculated following the expression given in de Strobel & Spite (1988), which takes into account the S/N ratio and the resolution of the spectra. For a resolution of $R = 48\,000$, and the typical S/N ratios mentioned in Section 2, the expected uncertainties in the equivalent widths are about 2–3 mÅ. To take into account the other components that contribute to the line-to-line scatter, we adopt the standard random errors, given by $\sigma_{\rm ran} = \sigma_{\rm obs}/\sqrt{n}$, where n is the number of lines considered to derive the abundance of a given chemical element X, and $\sigma_{\rm obs}$ is the standard deviation. In order to simplify the evaluation of the systematic errors associated with the stellar atmospheric parameters, we have assumed that their uncertainties are independent, following the methodology adopted in previous studies (e.g. de Castro et al. 2016; Cseh et al. 2018; Karinkuzhi et al. 2018; Roriz et al. 2021b).

The final abundance uncertainties, $\sigma_{\log\epsilon(\mathrm{X})}$, were calculated according to the following equation:

$$\sigma^2_{\log\epsilon(\mathrm{X})_\star} = \sigma^2_{\rm ran} + \left(\frac{\partial\log\epsilon}{\partial T_{\rm eff}}\right)^2\sigma^2_{T_{\rm eff}} + \left(\frac{\partial\log\epsilon}{\partial\log g}\right)^2\sigma^2_{\log g} + \left(\frac{\partial\log\epsilon}{\partial\xi}\right)^2\sigma^2_{\xi} + \left(\frac{\partial\log\epsilon}{\partial[\mathrm{Fe/H}]}\right)^2\sigma^2_{[\mathrm{Fe/H}]} + \left(\frac{\partial\log\epsilon}{\partial W_\lambda}\right)^2\sigma^2_{W_\lambda}, \quad (1)$$

similar to the formalism presented by McWilliam et al. (1995), where the partial derivatives correspond to variations in abundance when we change one parameter, keeping the others constant. Finally, the uncertainty in the [X/Fe] ratio is given by

$$\sigma^2_{[\mathrm{X/Fe}]} = \sigma^2_{\mathrm{X}} + \sigma^2_{\mathrm{Fe}}. \quad (2)$$

The partial derivatives in equation (1) were evaluated for the stars BD+03°2688 and HE 1255−2324. The results for HE 1255−2324 were also assumed for the other two targets, HE 0457−1805 and HE 2207−1746; this assumption is reasonable, since these two objects have uncertainties similar to HE 1255−2324. However, the $\sigma_{\rm ran}$ term was computed for each stars, when three or more lines were used in the abundance derivation.

The changes in $\log\epsilon(\mathrm{X})$ for the elements from sodium to lead are presented in Tables C1 and C3 of Appendix C, respectively, for BD+03°2688 and HE 1255−2324. From these tables, one can see that the abundances based on the neutral elements are more sensitive to the temperature variation that those based on singly ionized elements, which are more sensitive to surface gravity variation, such as seen in the variations of the abundances of Fe I and Fe II.

For the light elements, carbon, nitrogen, and oxygen, we followed the same procedure by varying the atmospheric parameters and then computing independently the abundance changes introduced by them, as shown in Tables C2 and C4, respectively, for BD+03°2688 and HE 1255−2324. The derived CNO abundances are not very sensitive to the variations of the microturbulent velocity, since weak lines were used for their determination. In addition, the uncertainties in one of the light elements may also affect the abundance of another light element, such as an uncertainty of the oxygen abundance affects the carbon abundance and vice versa. In the same way, uncertainties in the carbon abundance result in variation of nitrogen abundances, since the CN molecule lines are used for the N abundance determination. These changes are also presented in Tables C2 and C4. The uncertainty in the $^{12}\mathrm{C}/^{13}\mathrm{C}$ ratio was estimated from changes in the atmospheric parameters of HE 1255−2324, as shown in the last line of Table C4.

Table 4. Elemental abundances derived for BD+03°2688 and HE 0457−1805. The second column provides the solar photospheric abundances as recommended by Grevesse & Sauval (1998). The third and eighth columns give the abundances in the scale $\log \epsilon(\mathrm{H}) = 12$, and their respective dispersion among the lines of the elements with more than three available lines are shown in the fourth and ninth columns. The fifth and tenth columns give the information whether abundances were determined from spectrum synthesis technique (syn) or based on the equivalent width measurements; in this latter case, we provide the number of lines (n) used for the abundance determination. Abundances in the notations [X/H] and [X/Fe] are also provided. The $^{12}C/^{13}C$ isotopic ratio is given in the last line of the Table.

		BD+03°2688					HE 0457−1805				
Species	$\log \epsilon_\odot$	$\log \epsilon$	$\sigma_{\rm obs}$	n(#)	[X/H]	[X/Fe]	$\log \epsilon$	$\sigma_{\rm obs}$	n(#)	[X/H]	[X/Fe]
C (C_2)	8.52	7.67	–	syn	−0.85	+0.36	8.36	–	syn	−0.16	+0.03
N (CN)	7.92	6.90	–	syn	−1.02	+0.19	8.65	–	syn	+0.73	+0.92
O	8.83	7.58	–	syn	−1.25	−0.04	8.48	–	syn	−0.35	−0.16
Na I	6.33	4.89	0.09	04	−1.44	−0.23	6.70	0.09	03	+0.37	+0.56
Mg I	7.58	6.86	–	02	−0.72	+0.49	7.53	–	02	−0.05	+0.14
Al I	6.47	–	–	–	–	–	6.38	0.10	04	−0.09	+0.10
Si I	7.55	6.72	0.13	04	−0.83	+0.38	7.61	0.19	04	+0.06	+0.25
Ca I	6.36	5.55	0.10	11	−0.81	+0.40	6.43	0.08	06	+0.07	+0.26
Ti I	5.02	3.95	0.10	20	−1.07	+0.14	4.92	0.08	11	−0.10	+0.09
Fe I	7.50	6.29	0.13	65	−1.21	–	7.31	0.17	22	−0.19	–
Fe II	7.50	6.29	0.09	12	−1.21	–	7.32	0.15	06	−0.18	–
Cr I	5.67	4.35	0.14	10	−1.32	−0.11	5.50	0.09	07	−0.17	+0.02
Ni I	6.25	4.91	0.11	22	−1.34	−0.13	6.26	0.13	20	+0.01	+0.20
Rb I	2.60	–	–	–	–	–	2.85	–	syn	+0.25	+0.44
Sr I	2.97	3.03	0.21	03	+0.06	+1.27	3.80	–	02	+0.83	+1.02
Y II	2.24	1.86	0.17	06	−0.38	+0.83	3.35	0.02	03	+1.11	+1.30
Zr I	2.60	2.73	–	02	+0.13	+1.34	3.54	0.19	14	+0.94	+1.13
Nb I	1.42	–	–	–	–	–	2.62	0.10	syn	+1.20	+1.39
Mo I	1.92	–	–	–	–	–	3.47	0.18	04	+1.55	+1.74
Ru I	1.84	–	–	–	–	–	2.86	0.16	03	+1.02	+1.21
La II	1.17	1.28	0.10	05	+0.11	+1.32	2.75	0.14	04	+1.58	+1.77
Ce II	1.58	2.05	0.22	08	+0.47	+1.68	3.28	0.15	08	+1.70	+1.89
Nd II	1.50	1.88	0.14	16	+0.38	+1.59	3.20	0.12	14	+1.70	+1.89
Sm II	1.01	1.14	0.21	07	+0.13	+1.34	2.29	0.07	05	+1.28	+1.47
Eu II	0.51	0.00	–	syn	−0.51	+0.70	1.11	–	syn	+0.60	+0.79
Er II	0.93	–	–	–	–	–	2.70	0.26	03	+1.77	+1.96
W I	1.11	–	–	–	–	–	2.31	–	syn	+1.20	+1.39
Tl I	0.90	–	–	–	–	–	1.80	–	syn	+0.90	+1.09
Pb I	1.95	2.25	–	syn	+0.30	+1.51	3.25	–	syn	+1.30	+1.49
$^{12}C/^{13}C$		18		syn			20		syn		

5 RESULTS AND DISCUSSION

5.1 The position of the stars in the HR diagram and their luminosities

We estimate the stellar masses of the stars analysed in this work from their position in the $\log g$–$\log T_{\rm eff}$ diagram which are seen in Fig. 5. We used the evolutionary tracks of Girardi et al. (2000) for metallicities $Z = 0.001$ for BD+03°2688, $Z = 0.004$ for HE 2207−1746, and $Z = 0.008$ for HE 0457−1805 and HE 1255−2324, taking into account the results for $T_{\rm eff}$ and $\log g$ given in Table 2. We obtained a mass of 0.6–1 $M_\odot$ for BD+03°2688, ∼1.5–3 $M_\odot$ for HE 0457−1805, 1–2 $M_\odot$ for HE 1255−2324, and 0.6–1 $M_\odot$ for HE 2207−1746.

Their luminosities, along with uncertainties associated with the temperatures and surface gravities given in Table 2, were then obtained from the following relation:

$$\log\left(\frac{L_\star}{L_\odot}\right) = 4\log T_{\rm eff\star} - \log g_\star + \log\left(\frac{M_\star}{M_\odot}\right) - 10.61. \quad (3)$$

For BD+03°2688, HE 0457−1805, HE 1255−2324, and HE 2207−1746, the resulting luminosities according to the above equation are $\log(L_\star/L_\odot) = 2.22^{+0.31}_{-0.29}$, $2.28^{+0.44}_{-0.49}$, $1.35^{+0.34}_{-0.34}$, and $1.41^{+0.33}_{-0.33}$, respectively. To compute these luminosities based on distance, we adopted the bolometric correction (BC) relation of Alonso, Arribas & Martínez-Roger (1999), using the effective temperature and metallicity derived here, and $M_{\rm bol\odot} = +4.74$ (Bessell, Castelli & Plez 1998). The extinction was determined by using calibrations among $A_{\rm V}$, Galactic coordinates, and distances given by Chen et al. (1998). For the stars BD+03°2688 and HE 2207−1746, which are objects with high Galactic latitudes, the extinctions are very small; we have adopted the values $A_{\rm V} = 0.06$ and 0.07, respectively, according to the reddening map provided by the Infrared Science Archive (IRSA 2022). From the obtained distances, based in the parallaxes given by *Gaia* DR2 (Bailer-Jones et al. 2018), we derived $\log(L_\star/L_\odot) = 2.15$, 2.38, 1.44, and 1.67, respectively, for BD+03°2688, HE 0457−1805, HE 1255−2324, and HE 2207−1746, in good agreement with the luminosities derived from equation (3).

The luminosities of the target stars are all $\log(L_\star/L_\odot) \leq 2.1$, far below the threshold needed to be considered AGB stars, and therefore to become self-enriched by the elements of the *s*-process (see Section 5.4). According to Lattanzio (1986) and Vassiliadis & Wood (1993), the minimal luminosity for a star to be considered an AGB star is 1800 and 1400 $L_\odot$, or $\log(L_\star/L_\odot) = 3.26$ and 3.15, respectively.

An additional evidence that these stars are not currently experiencing internal *s*-process nucleosynthesis is the absence of technetium (Tc) in their atmospheres. Tc is an element with no stable isotope;

Table 5. Same as in Table 4, for the stars HE 1255−2324 and HE 2207−1746.

		HE 1255−2324					HE 2207−1746				
Species	$\log \epsilon_\odot$	$\log \epsilon$	σ_{obs}	n(#)	[X/H]	[X/Fe]	$\log \epsilon$	σ_{obs}	n(#)	[X/H]	[X/Fe]
C (C_2)	8.52	8.61	–	syn	+0.09	+0.40	8.49	–	syn	−0.03	+0.52
N (CN)	7.92	8.44	–	syn	+0.52	+0.83	8.25	–	syn	+0.33	+0.88
O	8.83	8.42	–	syn	−0.41	−0.10	8.33	–	syn	−0.50	+0.05
Na I	6.33	6.35	0.21	04	+0.02	+0.33	6.02	0.11	03	−0.31	+0.24
Mg I	7.58	7.49	0.10	04	−0.09	+0.22	7.36	0.04	04	−0.22	+0.33
Al I	6.47	6.37	0.02	04	−0.10	+0.21	6.08	0.08	03	−0.39	+0.16
Si I	7.55	7.30	0.07	03	−0.25	+0.06	7.29	0.12	04	−0.26	+0.29
Ca I	6.36	6.11	0.05	05	−0.25	+0.06	5.99	0.12	06	−0.37	+0.18
Ti I	5.02	4.87	0.07	10	−0.15	+0.16	4.67	0.12	15	−0.35	+0.20
Fe I	7.50	7.19	0.16	31	−0.31	–	6.95	0.15	37	−0.55	–
Fe II	7.50	7.20	0.15	05	−0.30	–	6.94	0.13	05	−0.56	–
Cr I	5.67	5.49	0.12	08	−0.18	+0.13	5.13	0.17	09	−0.54	+0.01
Ni I	6.25	6.16	0.07	13	−0.09	+0.22	5.73	0.03	13	−0.52	+0.03
Rb I	2.60	3.90	–	syn	+1.30	+1.61	2.45	–	syn	−0.15	+0.40
Sr I	2.97	4.11	0.24	03	+1.14	+1.45	3.35	–	02	+0.38	+0.93
Y II	2.24	3.54	0.14	04	+1.30	+1.61	2.93	0.10	04	+0.69	+1.24
Zr I	2.60	3.99	0.10	10	+1.39	+1.70	3.19	0.13	12	+0.59	+1.14
Nb I	1.42	3.22	0.15	syn	+1.80	+2.11	2.62	0.20	syn	+1.20	+1.75
Mo I	1.92	3.92	0.02	03	+2.00	+2.31	–	–	–	–	–
Ru I	1.84	3.03	0.03	03	+1.19	+1.50	2.38	0.10	03	+0.54	+1.09
La II	1.17	2.77	0.12	04	+1.60	+1.91	2.40	0.15	04	+1.23	+1.78
Ce II	1.58	3.06	0.16	07	+1.48	+1.79	2.73	0.15	08	+1.15	+1.70
Nd II	1.50	3.14	0.15	20	+1.64	+1.95	2.88	0.16	17	+1.38	+1.93
Sm II	1.01	2.31	0.11	04	+1.30	+1.61	1.78	0.12	04	+0.77	+1.32
Eu II	0.51	1.40	–	syn	+0.89	+1.20	0.91	–	syn	+0.40	+0.95
Er II	0.93	3.37	0.16	04	+2.44	+2.75	2.16	–	01	+1.23	+1.78
W I	1.11	2.74	–	syn	+1.63	+1.94	2.06	–	syn	+0.95	+1.50
Tl I	0.90	2.35	–	syn	+1.45	+1.76	1.90	–	syn	+1.00	+1.55
Pb I	1.95	3.05	–	syn	+1.10	+1.41	2.95	–	syn	+1.00	+1.55
$^{12}C/^{13}C$		18		syn			≥ 40.0		syn		

the radioactive *s*-nuclide ^{99}Tc has a half-live $T_{1/2} \sim 2.1 \times 10^5$ yr. Therefore, its detection in the stellar spectra is a remarkable signature of the *s*-process currently taking place inside the stars. We searched for Tc lines in the spectra of the program stars. In Fig. B4, we show the regions close to the Tc I lines at 4238.19, 4262.27, and 5924.47 Å, commonly used to its detection. The Tc I transitions around 4238.19 and 5924.47 Å are clearly absent; the feature at 4262.27 Å, as already reported by Van Eck & Jorissen (1999), has a Nd II contribution at 4262.228 Å. Then, as an exercise, we computed synthetic spectra close to this region (see middle panels of Fig. B4), where we note that the absorption in 4262.2 Å is due to the high amount of Nd present in these stars. Therefore, the non-detection of Tc in our targets is a further clue that *s*-process is not currently taking place inside these stars, and supports the hypothesis of the mass transfer mechanism to explain the overabundance of the *s*-process observed in these systems.

5.2 Radial velocity

In this section, we will discuss the binary status of the program stars, a fundamental requirement to support the mass transfer scenario as origin of their chemical peculiarities.

BD+03°2688 displays properties of a halo star; although its radial velocity is low (+32.8 km s^{-1}), it is a metal-poor star and has a high Galactic latitude. In addition, BD+03°2688 satisfies several pre-requisities to be considered a CH star: it is a *s*-process enriched star (as we will see in Section 5.4, BD+03°2688 has [*s*/Fe] = 1.36, where [*s*/Fe] is the averaged *s*-process abundance), with C/O = 1.23 (see Section 5.3.1), and absolute magnitude $M_V = -0.07 \pm 0.01$, which is slightly lower than the typical values among the CH stars (according to Table IV of Hartwick & Cowley 1985, CH stars have M_V values between −0.25 and −2.2). Like the CH stars, BD+03°2688 should be a binary system.

As seen in Section 5.1, BD+03°2688 is not luminous enough to be considered an AGB star, in order to account for the observed overabundance of carbon and the elements created by the *s*-process. Therefore, the observed heavy-element overabundance could be due to a mass transfer happened in the past. In Table 6, we list all known heliocentric radial velocity measurements for BD+03°2688 available in the literature and determined in this work. Their mean value is 33.01 ± 0.21 km s^{-1} ($\sigma = 0.64$ km s^{-1}), essentially constant to within the stated measurement uncertainties. A similar conclusion was also found by Jorissen et al. (2005). The absence of the radial velocity variations may also be due to the predominance of the transverse velocity in the space velocity of this star. In Fig. 6, we show the radial velocity measurements obtained by Jorissen et al. (2005) and the two our values of 32.64 ± 0.29 and 34.36 ± 0.19 km s^{-1} obtained in this study. Therefore, a systematic radial velocity monitoring is necessary to confirm the possible binary nature of BD+03°2688.

For the stars HE 0457−1805, HE 1255−2324, and HE 2207−1746, the heliocentric radial velocities were also determined based on Doppler shifts of ten absorption lines. For HE 0457−1805, we obtained 61.22 ± 0.24 km s^{-1}, which is in the range between 60.92 km s^{-1} and 73.99 km s^{-1} due to the variation of its binary period of 2724 d (Pourbaix et al. 2004; see also Jorissen et al. 2016). For HE 1255−2324, we obtained two different radial velocities: 37.25 ± 0.26 km s^{-1}, from the spectrum obtained at 2010

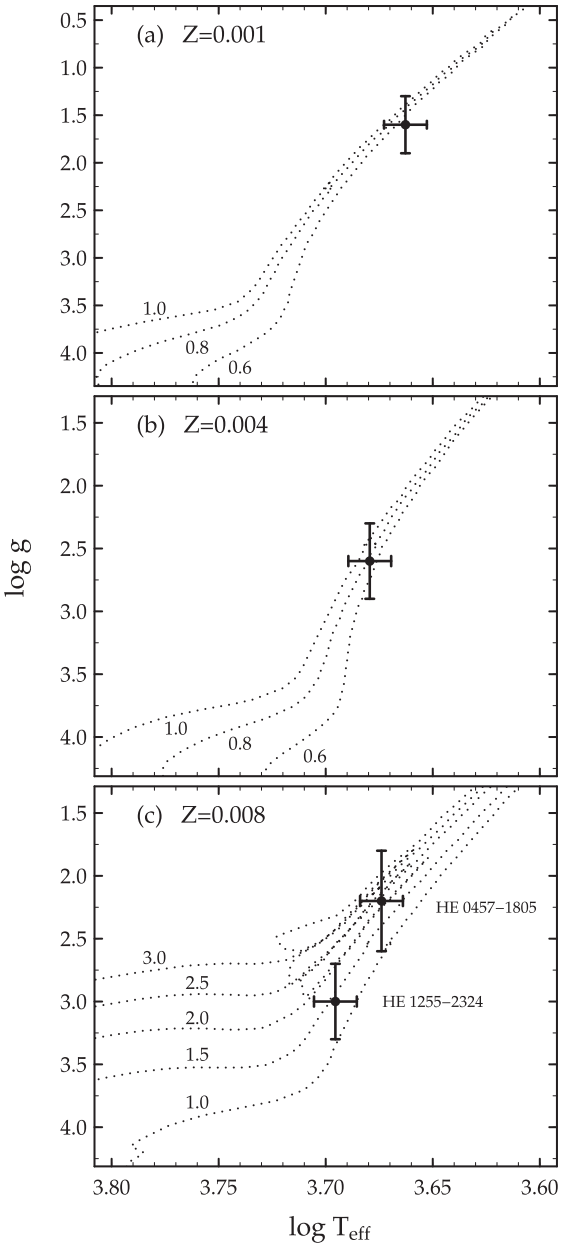

Figure 5. Position of the stars BD+03°2688 (panel a), HE 2207−1746 (panel b), HE 0457−1805, and HE 1255−2324 (panel c) in the log g–log $T_{\rm eff}$ diagram. The dotted curves are evolutionary tracks taken from Girardi et al. (2000), where the numbers correspond to stellar masses in units of solar mass ($M_{\odot}$).

May 4, and 18.21 ± 0.21 km s^{-1}, from the spectrum obtained at 2010 August 1. In fact, HE 1255−2324 presents a variation of its radial velocity. The radial velocity experiment (RAVE; Kunder et al. 2017) gives for this object 20.747 ± 2.184 km s^{-1}. Finally, for HE 2207−1746, there is no previous radial velocity determination; for this system, we obtained −8.01 ± 0.21 km s^{-1}.

5.3 Light elements

5.3.1 C, N, O, and carbon isotopic ratios

Fig. 7 shows the [C/Fe], [N/Fe], and [O/Fe] ratios for the stars analysed this work in comparison with data for field giant stars

Table 6. Date of observation, Modified Julian Date (MJD), and the known values for the observed heliocentric radial velocity (Vr) of the star BD+03°2688.

Date of observation	MJD	Vr (km s^{-1})	Error	Ref.
1993 Apr. 8	49086.481	33.16	0.43	1
1994 Mar. 5	49417.506	32.35	0.47	1
1994 Apr. 3	49446.510	32.33	0.44	1
1994 May 14	49487.388	33.00	0.47	1
1995 Feb. 3	49752.658	33.52	0.52	1
1995 Mar. 30	49807.506	32.64	0.71	1
1995 Dec. 20	50072.729	33.07	0.46	1
2007 Apr. 4	54194.146	32.64	0.29	2
2016 Mar. 18	57465.155	34.36	0.19	2

Note. *References:* (1) Jorissen et al. (2005); (2) This work.

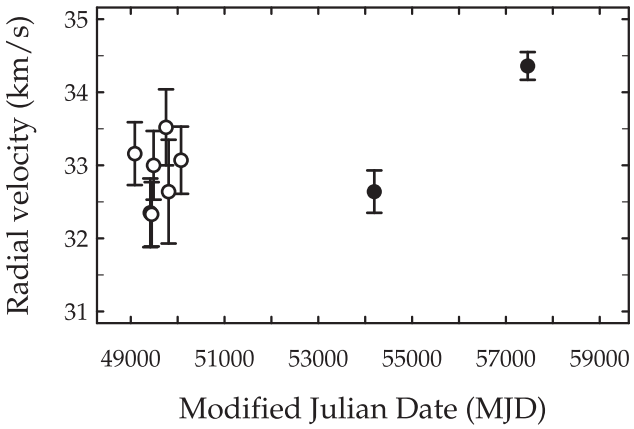

Figure 6. Radial velocity of BD+03°2688 as a function of the Modified Julian Date (MJD). Open points are data taken from Jorissen et al. (2005); the filled points (this work) at MJD = 54194.146 and 57465.155 are data observed with the FEROS spectrograph at 2007 April 4 and 2016 March 18, respectively.

and other classes of chemically peculiar stars, as identified in the figure caption. Three out of the four program stars show carbon enrichment with [C/Fe] ratios above those observed for field stars, as typically found in barium stars and CH stars; they are BD+03°2688, HE 2207−1746, and HE 1255−2324, with [C/Fe] = 0.36, 0.52, and 0.40, respectively. For HE 0457−1805, the [C/Fe] ratio is just slightly above the average trend of the field stars. The excess of carbon can be explained in terms of mass transfer from a previous carbon enriched AGB star, as a result of the helium burning and the occurrence of the third dredge-up.

From the middle panel of Fig. 7, we see that the stars HE 0457−1805, HE 1255−2324, and HE 2207−1746 present a nitrogen abundance higher than the main trend of field stars, in accordance with high [N/Fe] ratios observed in some barium stars. The observed nitrogen overabundance may be due to the occurrence of the first dredge-up in the barium giant (Barbuy et al. 1992; Allen & Barbuy 2006; Drake & Pereira 2008). Interesting, BD+03°2688 does not show a high [N/Fe] ratio, usually seen in chemically peculiar stars enriched by the mass transfer down to metallicity ≈−1.0. None the less, its [N/Fe] ratio is similar to that of the other metal-poor barium star, HD 123396 (Allen & Barbuy 2006), thus indicating that in both stars mixing was not very efficient, similar to a phenomena already seen, but at lower metallicities, in possible single stars (Spite et al. 2005, 2006). BD+03°2688 has also a [O/Fe] ratio lower than

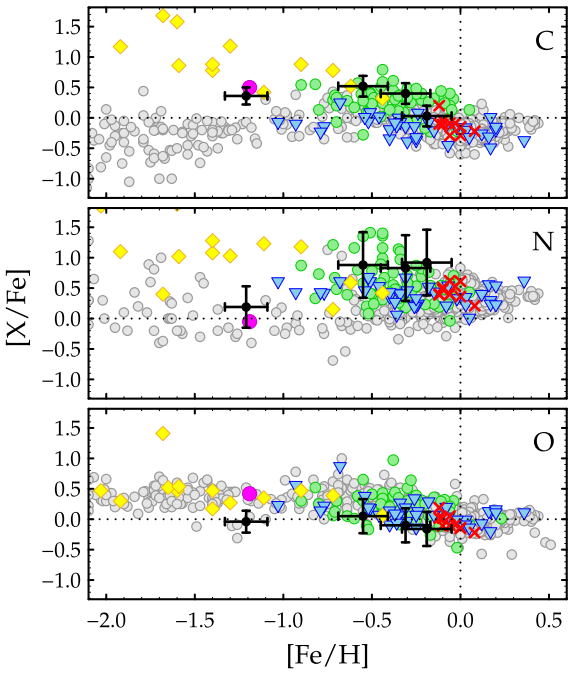

Figure 7. Observed [C, N, O/Fe] abundance ratios as a function of metallicity for the stars analysed in this study (black dots with error bars) along with data for field giant stars (grey dots, taken from Gratton & Ortolani 1986; Barbuy 1988; Barbuy & Erdelyi-Mendes 1989; Sneden et al. 1991; Kraft et al. 1992; Shetrone 1996; Carretta, Gratton & Sneden 2000; Gratton et al. 2000; Simmerer et al. 2004; Spite et al. 2005; Mishenina et al. 2006; Luck & Heiter 2007; Smiljanic et al. 2009; Alves-Brito et al. 2010; Tautvaišienė et al. 2010, 2013, 2015, 2016; Santrich, Pereira & Drake 2013; Szigeti et al. 2018; Takeda et al. 2019), barium stars (green dots, taken from Smith 1984; Barbuy et al. 1992; Allen & Barbuy 2006; Pereira & Drake 2009; Karinkuzhi et al. 2018; Shejeelammal et al. 2020), CH stars (yellow diamonds, taken from Vanture 1992a, b; Pereira & Drake 2009; Pereira et al. 2012; Goswami et al. 2016; Purandardas et al. 2019), S-type symbiotic stars (blue triangles, taken from Gałan et al. 2016, 2017), and M giant stars (red crosses, taken from Smith & Lambert 1985). The barium star HD 123396 is shown by the magenta dot (see discussion in the text).

other field stars in the same range of metallicity, similar to the star BD + 30°2611 ([O/Fe] = +0.04; Kraft et al. 1992) of the same metallicity. Other chemically peculiar stars also have low [O/Fe] ratios considering their metallicities (Vanture 1992b).

Dwarf stars do not exhibit nitrogen enrichment, and in the metallicity range between −2.0 and +0.3, the [N/Fe] ratio remains close to zero (Tomkin & Lambert 1984). However, as the star becomes a red giant, the first dredge-up brings nuclear processed material from its interior layers, changing the stellar surface composition; as a result, there is a depletion of ^{12}C and an enrichment of ^{14}N (Lambert 1981). Therefore, the sum $\log\epsilon$(C+N) should remain unchanged. The sample of giants stars analysed by Luck & Heiter (2007) shows that, in fact, the $\log\epsilon$(C+N) did not significantly changed as these stars became giants. For that sample, we found a mean of 8.66 ± 0.17 for $\log\epsilon$(C+N), for a metallicity range between −0.6 and +0.3; this value is only +0.04 higher than the $\log\epsilon(\mathrm{C+N})_\odot$, for the solar carbon and nitrogen abundances given in Column 2 of Tables 4 and 5. Fig. 8 shows $\log\epsilon$(C+N) as a function of metallicity, where the black dashed line is the solar scaled composition, and includes data for $\log\epsilon$(C+N) from the giants analysed by Luck & Heiter, symbiotic stars, M giants, barium stars, and CH stars. Fig. 8 also shows how $\log\epsilon$(C+N) behaves for the stars studied in this work. HE 0457−1805, HE 1255−2324, and HE 2207−1746 present an

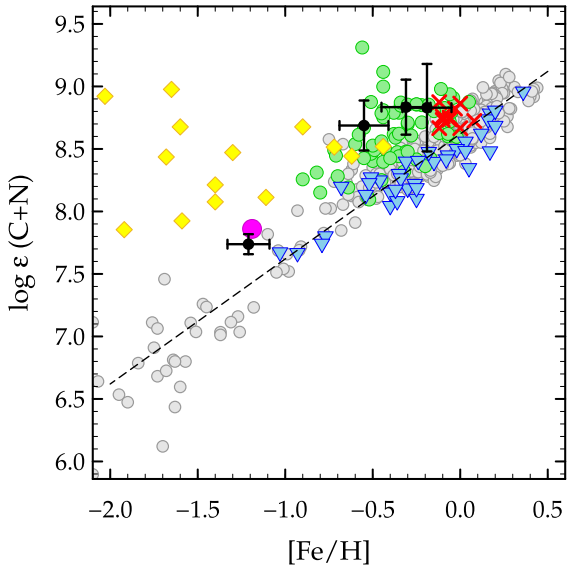

Figure 8. Observed C + N abundance in the notation of $\log\epsilon(\mathrm{C+N})$ as a function of metallicity. Symbols have the same meaning as in Fig. 7. The black dashed line shows initial CN abundance for a given metallicity. The barium star HD 123396 is shown by the magenta dot (see discussion in the text).

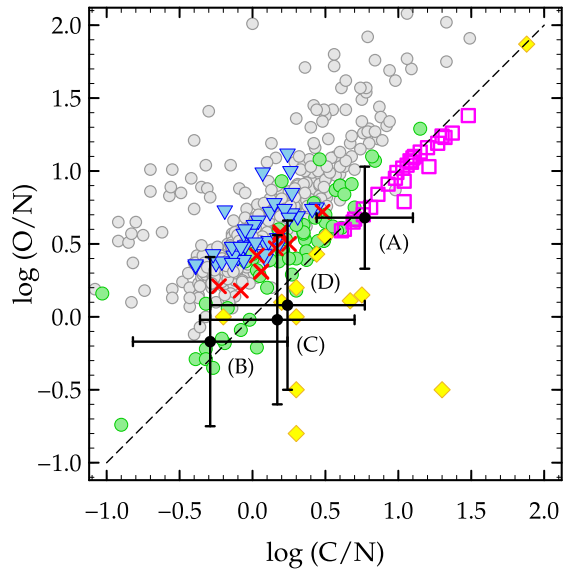

Figure 9. Abundance ratios by number O/N against C/N. Symbols have the same meaning as in Fig. 7. We have added to this plot abundance data for the classical carbon stars (magenta squares, taken from Lambert et al. 1986). The program stars, BD+03°2688, HE 0457−1805, HE 1255−2324, and HE 2207−1746, are, respectively, labelled as (A), (B), (C), and (D).

excess of carbon and nitrogen, sharing the same position where we found barium stars in the diagram. Taken together, the excess of carbon is best explained in terms of mass transfer, while the excess of nitrogen is due the occurrence of the first dredge-up in the barium giant. The position of BD+03°2688 in this diagram also indicates that this star presents an excess of $\log\epsilon$(C+N), but this is due to excess of carbon only since it has a low [N/Fe] ratio like the barium star HD 123396 (Allen & Barbuy 2006).

Fig. 9 shows the stars analysed in this work in the log O/N ratio *versus* the log C/N ratio diagram for the same classes of stars shown in previous figures. Further, we added in Fig. 9 the

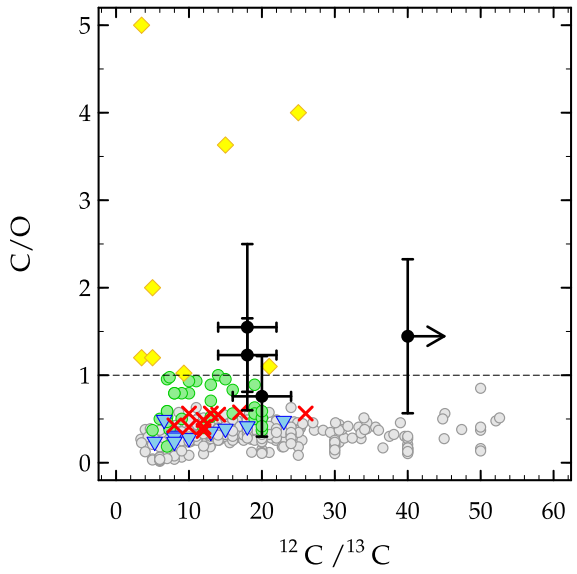

Figure 10. Carbon isotopic ratio, ^{12}C/ ^{13}C, against C/N ratio for the program stars. Symbols have the same meaning as in Fig. 7.

classical Galactic carbon stars with the aim to show where the carbon enriched objects are located. Carbon rich objects lie below the black dashed line that represents C/O = 1, from which we can better set the evolutionary status of the stars analysed in this work. In this diagram, the star HE 0457−1805 (C/O = 0.76), labelled as (B), shares the same region where other barium stars are found, while BD+03°2688 (C/O = 1.23), HE 1255−2324 (C/O = 1.55), and HE 2207−1746 (C/O = 1.45), respectively, labelled as (A), (C), and (D) in the diagram, lie on the side of carbon rich objects. Therefore, HE 2207−1746 (D) and HE 1255−2324 (C) are likely metal-rich CH stars, and spectroscopically can be confused as 'barium stars'. This explains why they may have the same position of the barium stars in previous Fig. 8.

In Fig. 10, we plot the C/O ratio *versus* the ^{12}C/ ^{13}C isotopic ratio for the program stars, along with data for field giant stars and other chemically peculiar stars. The results determined for BD+03°2688, HE 0457−1805, and HE 1255−2324 are in accordance with other ^{12}C/ ^{13}C isotopic ratios already determined for barium stars (Smith 1984; Barbuy et al. 1992; Pereira & Drake 2009; Karinkuzhi et al. 2018). Low ^{12}C/ ^{13}C isotopic ratios in combination with high [N/Fe] ratios follow the expectations given by the first dredge-up (Lambert 1981). HE 2207−1746, on the other side, has a high nitrogen abundance ([N/Fe] = + 0.88) and a ^{12}C/ ^{13}C isotopic ratio with value higher than 40, not commonly seen among the barium stars and CH stars, which may be due to the mass transfer from an AGB carbon star with high ^{12}C/ ^{13}C.

According to the classical theory of stellar evolution (Iben 1964, 1965, 1967), the ^{14}N/ ^{12}C abundance ratio and the ^{12}C/ ^{13}C isotopic ratio on the stellar surface change due to the dredging-up CN-processed material, caused by a deepening of the convective zone of the star approaching the red giant branch phase (first dredge-up). Comparison with observational data and further development of the theory of the first dredge-up are presented in Lambert (1981), Sneden (1991), Charbonnel (1994, 1995), Boothroyd & Sackmann (1999), Gratton et al. (2000), among others. The origin of the nitrogen in extremely metal-poor giants was studied by Spite et al. (2005). The authors found that the more evolved giants of their sample show evidence of CN cycling as well as strong Li dilution which confirms mixing by the first dredge-up at lower metallicities.

5.3.2 *Elements from sodium to nickel*

In Fig. 11, we show the [X/Fe] abundance ratios for sodium, magnesium, aluminum, silicon, calcium, titanium, chromium, and nickel in comparison with data for field giants stars, barium stars, and CH stars. It can be seen that the target stars behave similar to the field stars, as well as the barium stars and CH stars. Sodium, aluminum, magnesium, silicon, calcium, and titanium are mainly produced in the Galaxy by hydrostatic burning in massive stars of initial masses roughly 10–30 $M_{\odot}$ (Woosley & Weaver 1995). Sodium, aluminum, and magnesium are produced by hydrostatic carbon burning, although magnesium can also be produced by neon burning. Silicon and calcium can be produced by hydrostatic oxygen burning. Type II supernova explosions may also originate large amounts of silicon and calcium. Titanium is produced by oxygen burning but can also be produced by Type Ia supernova events (Woosley & Weaver 1995). Because of the atomic number of titanium, Timmes, Woosley & Weaver (1995) considered this element as an iron-peak element in their analysis of the chemical evolution of the Galaxy. Iron, chromium, and nickel are formed in Type I supernova events and also during the final stages of the massive stars (Timmes et al. 1995); therefore, these elements should follow the same trend as the iron abundance, as we can see in Fig. 11.

Compared to the field stars, HE 0457−1805 presents a high [Na/Fe] ratio of +0.56. Field stars with high sodium abundances, that is, those with [Na/Fe] ratios higher than +0.5 to +0.7 are rare (Pereira et al. 2019a). Stars with [Na/Fe] ratios with values closer to +1.0 can be considered 'second generation of globular cluster star' that has escaped from globular cluster and now is a field halo star (Pereira et al. 2019b). Field giant stars that exhibit sodium enrichment up to ≈+0.40 have already been reported, but only in a few cases. In the samples of the studied stars by Luck & Heiter (2007) and Takeda, Sato & Murata (2008), only 3–4 per cent of stars have [Na/Fe] ratios between +0.30 and +0.40. HD 188650, analysed by Takeda et al., with a metallicity of −0.67, has a high [Na/Fe] ratio of +0.62, which is only 0.3 per cent of the total sample. Karinkuzhi & Goswami (2014) also reported a high [Na/Fe] ratio for this star (+0.76). These authors also rejected HD 188650 as a CH star due to its low heavy-element abundance. This star was classified as 'low velocity CH star' by Bidelman (1957), i.e. stars that have enhanced CH bands but with low radial velocities, contrary to the classical halo CH metal-poor stars which have high radial velocities. Vanture & Wallerstein (1999), in their analysis of the stars in Hertzsprung Gap, concluded that these low velocity CH stars with their mild metal deficient 'will enhance the appearance of the CH band on low-resolution spectra'. Since the stars that are in the Hertzsprung Gap have just left the main sequence, probably their high [Na/Fe] ratios are owed to NeNa cycle (Denisenkov & Ivanov 1987) in its hydrogen-burning core while the star was still on the main sequence. In barium stars, sodium enrichment at a similar quantity as seen is HE 0457−1805 has already been reported (Antipova et al. 2004; de Castro et al. 2016; Karinkuzhi et al. 2018). Such enrichments can be currently explained through the reaction ^{22}Ne(p, γ)^{23}Na in the hydrogen burning shells (Mowlavi 1999) in the previous AGB companion stars.

5.4 Heavy elements

The bulk of the chemical elements beyond the iron group is synthesized via neutron-capture nuclear reactions, as previously mentioned, since neutrons do not need to overcome the Coulomb barrier to penetrate into atomic nuclei. Depending on the time-scales involved between neutron captures and β-decays of the radioactive nuclei, the mechanism can operate into two extreme regimes, the so

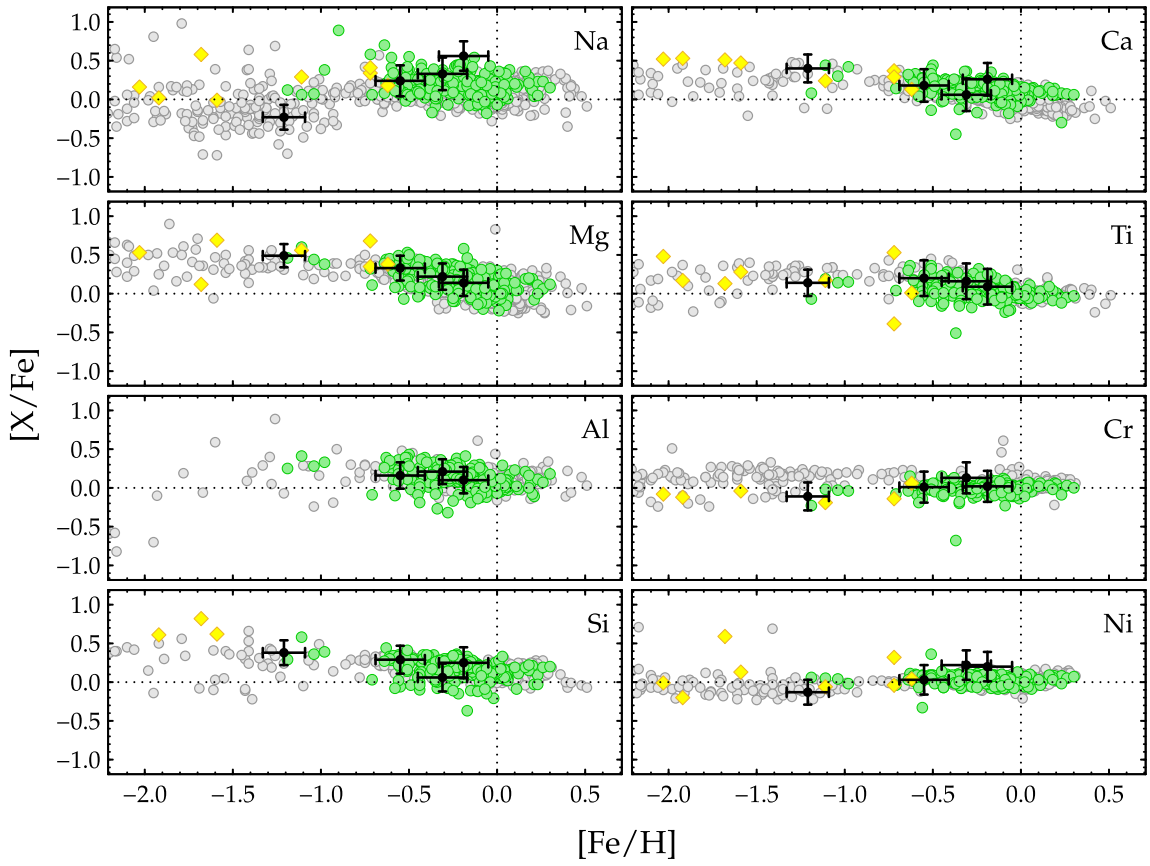

Figure 11. Observed [X/Fe] abundance ratios as a function of metallicity for the stars analysed in this study (black dots with error bars) along with data for field giant stars (grey dots, taken from Kraft et al. 1992; Shetrone 1996; Carretta et al. 2000; Gratton et al. 2000; Johnson 2002; Mishenina et al. 2006; Luck & Heiter 2007; Zhang et al. 2009; Smiljanic et al. 2009; Alves-Brito et al. 2010; For & Sneden 2010; Santrich et al. 2013; Ishigaki et al. 2018; Szigeti et al. 2018; Takeda et al. 2019), barium stars (green dots, taken from Allen & Barbuy 2006; Pereira et al. 2011; de Castro et al. 2016; Karinkuzhi et al. 2018; Shejeelammal et al. 2020), and CH stars (yellow diamonds, taken from Pereira & Drake 2009; Pereira et al. 2012; Goswami et al. 2016; Purandardas et al. 2019).

called *s*-process and *r*-process, which require different astrophysical conditions. The physical conditions required by the *s*-process are found within the He-rich region between the H-burning shell and He-burning shell, which are alternately activated during the TP-AGB phase; the *s*-process is powered by neutron density of the order of 10^{7-12} cm^{-3} (e.g. Abia et al. 2001; Busso et al. 2001; Cristallo et al. 2011; van Raai et al. 2012; Fishlock et al. 2014) and evolves close to the valley of β stability. The *r*-process, on the other hand, is associated with explosive events, such as those found in supernovae and neutron star mergers (see Cowan et al. 2021, for a recent review), where high neutron densities ($\gtrsim 10^{20}$ cm^{-3}) are needed.

Both *s*-process and *r*-process contribute to the cosmic abundances of the elements from iron to bismuth. We show in Table 7 the *s*-process contribution to the observed Solar system material for the chemical elements considered in this study; these data were taken from different works in literature. Additionally, in Fig. 12, we compare the observed [X/Fe] abundance ratios derived for the targets of this work with data available in literature for field giant stars, barium stars, CH stars, CEMP stars, and post-AGB stars, where we can clearly see the *s*-rich nature of the program stars, i.e. large overabundances of *n*-capture elements compared to the normal giant stars of the Galaxy (grey dots in Fig. 12). Such characteristics will be discussed below. As we previously noted, these stars have not yet experienced the *s*-process nucleosynthesis in their interior, so that the presence of heavy elements in their atmospheres is probably a consequence of the mass transfer from a former AGB star.

Table 7. Contribution (per cent) of the *s*-process to the Solar system material as provided by different works in literature for the neutron-capture elements considered in this study.

Species	S96	A99	B00	B14
Rb	97	22	50	18
Sr	85	85	89	69
Y	72	92	72	72
Zr	83	83	81	66
Nb	68	85	68	56
Mo	68	50	68	39
Ru	39	32	39	29
La	75	62	75	76
Ce	77	77	81	84
Nd	47	56	47	58
Sm	24	29	34	31
Eu	3	6	3	6
Er	16	17	16	20
W	54	56	54	62
Tl	66	76	66	71
Pb	79	46	79	87

Note. References: (S96) Sneden et al. (1996); (A99) Arlandini et al. (1999); (B00) Burris et al. (2000); (B14) Bisterzo et al. (2014).

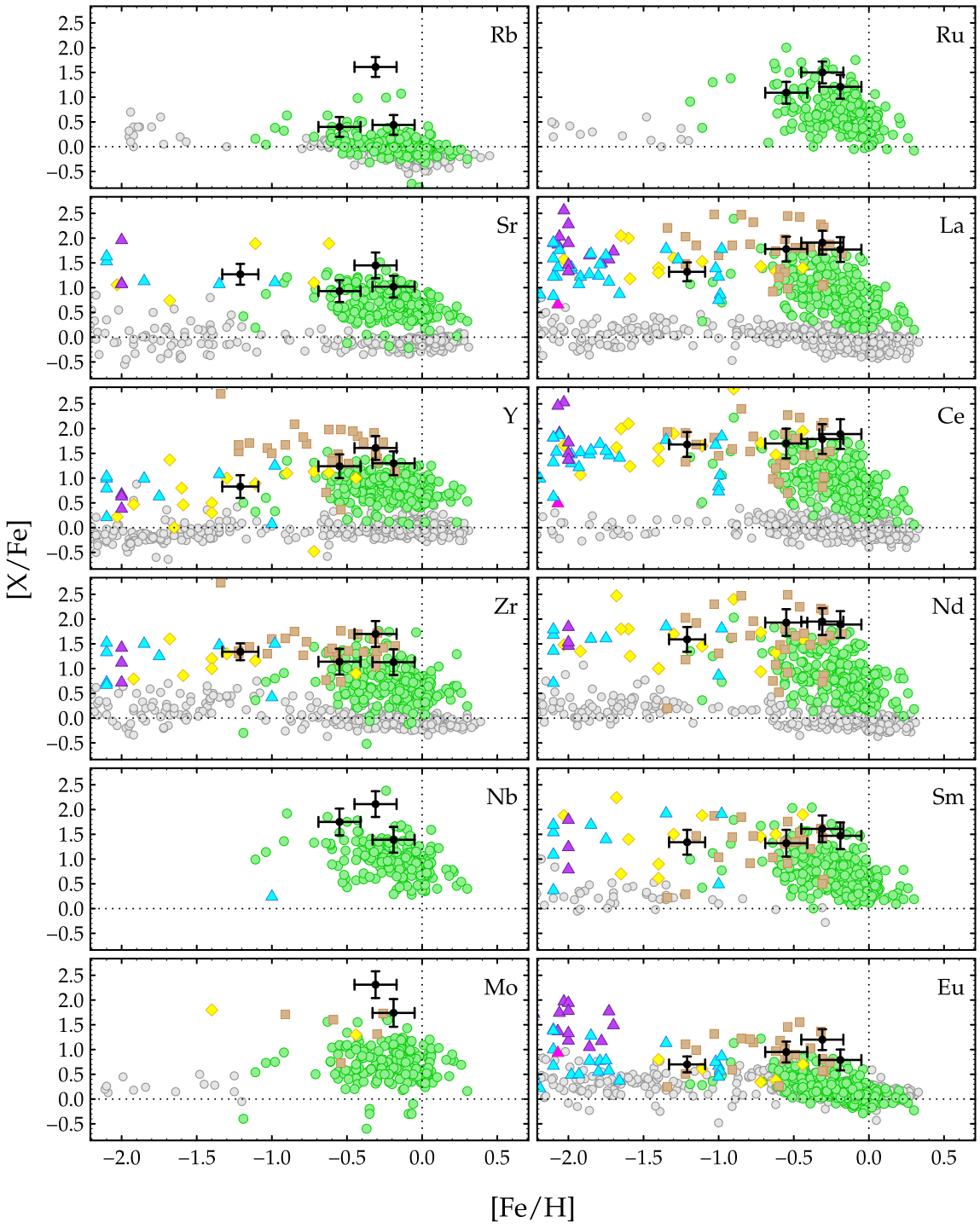

Figure 12. Observed [X/Fe] abundance ratios as a function of metallicity for the stars analysed in this study (black dots with error bars) along with data for field giant stars (grey dots, taken from Gratton & Sneden 1994; Tomkin & Lambert 1999; Burris et al. 2000; Mishenina & Kovtyukh 2001; Johnson 2002; Luck & Heiter 2007; Mishenina et al. 2007; Zhang et al. 2009; For & Sneden 2010; Santrich et al. 2013; Hansen, Andersen & Christlieb 2014; Ishigaki et al. 2018; Forsberg et al. 2019; Abia et al. 2021; Takeda 2021), barium stars (green dots, taken from Allen & Barbuy 2006; Allen & Porto de Mello 2007; Karinkuzhi et al. 2018; Shejeelammal et al. 2020; Roriz et al. 2021a, b), CH stars (yellow diamonds, taken from Vanture 1992c; Pereira & Drake 2009; Pereira et al. 2012; Goswami et al. 2016; Purandardas et al. 2019), and post-AGB stars (brown squares, taken from Van Winckel & Reyniers 2000; Reyniers et al. 2004; De Smedt et al. 2012, 2015, 2016; van Aarle et al. 2013). Triangles are data for CEMP-*s* (cyan), CEMP-*r* (magenta), and CEMP-*r*/*s* (purple) stars, taken from Masseron et al. (2010) and Karinkuzhi et al. (2021).

In Fig. 13, we show the [La/Fe] *versus* [Eu/Fe] plane. The location of the stars in this diagram evidences their *s*-rich or *r*-rich nature, since La and Eu are representative elements of the *s*-process (∼75 per cent) and *r*-process (≳ 95 per cent), respectively. We have also added to this plot abundance data available for barium stars, CH stars, CEMP stars, and post-AGB stars. As one can observe in Fig. 13, the subclasses of the CEMP stars occupy different regions in this plot. While CEMP-*r* stars (magenta triangles) are found on

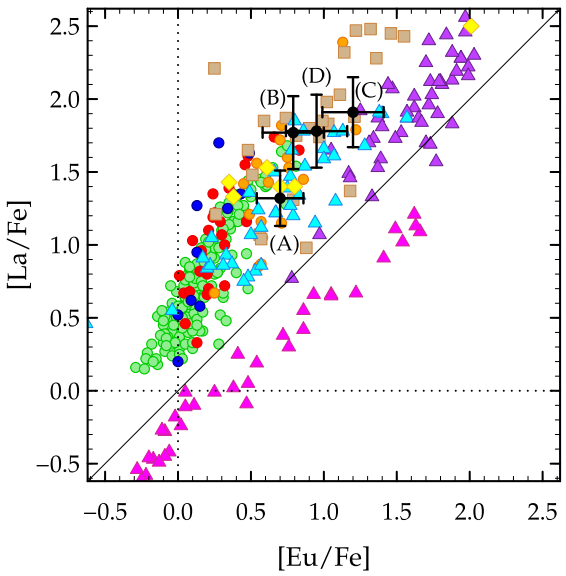

Figure 13. [La/Fe] *versus* [Eu/Fe] plane showing the distribution of the program stars (black dots with error bars), BD+03°2688 (A), HE 0457−1805 (B), HE 1255−2324 (C), and HE 2207−1746 (D). Symbols have the same meaning as in Fig. 12. However, for the barium stars, we adopt a colour code to identify the objects analysed by Allen & Barbuy (2006, red), Karinkuzhi et al. (2018, orange), Shejeelammal et al. (2020, blue), and Roriz et al. (2021b, green).

the *r*-rich side of this diagram, CEMP-*s* stars (cyan triangles) are located on the *s*-rich side, lying close to barium stars, CH stars, and post-AGB stars. Note that CEMP-*r*/*s* stars (purple triangles), in turn, represent a different population in this plane. The targets analysed in this study, BD+03°2688 (A), HE 0457−1805 (B), HE 1255−2324 (C), and HE 2207−1746 (D), show high levels of *s*-enrichment, with [*s*/Fe] = 1.36, 1.36, 1.77, and 1.38, respectively, where [*s*/Fe] is the average abundance of the *s*-elements, computed from the elemental abundances of Rb, Sr, Y, Zr, Nb, Mo, Ru, La, Ce, Nd, W, Tl, and Pb. As expected, these stars are found on the *s*-rich side of the [La/Fe]*versus* [Eu/Fe] diagram. In particular, HE 1255−2324 (C) falls very close to the region where CEMP-*r*/*s* stars are found. So far, similar characteristics were reported by Karinkuzhi et al. (2018) for the barium star HD 100503 ([La/Fe] = 1.79; [Eu/Fe] = 1.22), with [*s*/Fe] = 1.46 at [Fe/H] = −0.72.

Recently, Karinkuzhi et al. (2021) have proposed a $d_{\rm rms}$ distance, in dex, of the observed abundance pattern from the standard solar *r*-process abundance profile, in order to constraint among the different classes of CEMP stars. The novelty of this metric lies in the fact that it is not based only on two elemental abundances (commonly La and Eu), but in a set of *N* elemental abundances. As advantage, this new approach considers at the same time all the abundance data derived for the heavy elements, becoming more refined as more chemical elements are taken into account. By definition, the $d_{\rm rms}$ quantity is null for the *r*-element europium, that is assumed as a normalizing element. In summary, the more the *s*-process contribution dominates the stellar abundance pattern, the further away from the solar *r*-process profile the observed data set will be, reflecting in greater $d_{\rm rms}$ distance values. We refer the reader to section 5 of Karinkuzhi et al. (their equations 4 and 5) for further details.

In Roriz et al. (2021b), we reported the average $d_{\rm rms}$ values for barium stars (1.15) and field stars (0.50). In this study, we computed $d_{\rm rms}$ = 1.29, 1.25, 1.21, and 1.10 dex for BD+03°2688, HE 0457−1805, HE 1255−2324, and HE 2207−1746, respectively. These values, indeed, confirm the strong *s*-rich nature of the program stars. In Fig. B5, similar to fig. 8 of Roriz et al. (2021b), we show a plot of the [*s*/Fe] ratio against $d_{\rm rms}$ for the systems analysed in this work, along with data for field stars, barium stars, CH stars, and post-AGB stars, where we can see that our stars exhibit [*s*/Fe] and $d_{\rm rms}$ on the top of the values observed in barium stars.

As far as the neutron source of the *s*-process is concerned, the $^{13}C(\alpha, n)^{16}O$ and $^{22}Ne(\alpha, n)^{25}Mg$ reactions provide the free neutrons needed to drive the *s*-process. For low-mass (1–4 $M_\odot$) AGB stars, the $^{13}C(\alpha, n)^{16}O$ reaction is the main neutron source, effectively activated during the interpulse period, at $T \sim 10^8$ K, under radiative conditions, within a so-called ^{13}C pocket formed in the He-rich intershell region, whereas the ^{22}Ne source is marginally activated for this mass range. For more massive (4–8 $M_\odot$) AGB stars, the $^{22}Ne(\alpha, n)^{25}Mg$ reaction becomes the main neutron source, activated during the thermal pulses, at $T \geq 3 \times 10^8$ K, under convective conditions, releasing higher neutron densities. The element rubidium is an useful chemical species to probe and constraint the main neutron source of the *s*-process. This is due to the fact that the amount of Rb produced depends on the unstable isotopes ^{85}Kr ($T_{1/2} \sim 11$ yr) and ^{86}Rb ($T_{1/2} \sim 19$ d) which act as branching points along the *s*-process path (see fig. 1 of van Raai et al. 2012). High neutron densities are able to open the branches, favouring the production of ^{87}Rb, which has a magic number of neutrons and a low neutron-capture cross-section; therefore, once ^{87}Rb is produced, it tends to accumulate. For low neutron densities, the branching points are closed and the ^{85}Rb production is favoured, which has a neutron-capture cross-section higher than ^{87}Rb. The $^{85}Rb/^{87}Rb$ isotopic ratio would give us direct insights about the physical conditions of the *s*-process, however, this quantity cannot be evaluated from spectroscopic data. However, the abundance ratios between Rb and its neighbourhood elements, such as Sr and Zr, can be used with the same purpose; we will discuss this further in Section 5.5, in the light of the *s*-process models.

In Fig. 14, where we consider the Rb and Zr abundances, the data derived in this study are compared with data recently reported in literature for barium stars. Additionally, Fig. 14 shows the observed ranges of the [Rb/Fe] and [Zr/Fe] ratios for AGB stars of the Galaxy and Magellanic Clouds. The magenta box and grey shaded region drawn in this plot delimit the observed values for AGB stars of low- and intermediate-mass, respectively (García-Hernández et al. 2006, 2009). In the light of the *s*-process nucleosynthesis models, it is known that low-mass (∼2–3 $M_\odot$) polluting AGB stars are able to reproduce the abundance profiles observed in barium stars (e.g. Karinkuzhi et al. 2018; Shejeelammal et al. 2020; Roriz et al. 2021a; Stancliffe 2021; Cseh et al. 2022). A discussion of the physics of mass transfer is beyond the scope of this study, none the less, the interested reader is referred to the works of Liu et al. (2017) and Chen, Ivanova & Carroll-Nellenback (2020), for instance, who performed 3D hydrodynamical simulations to predict the mass-accretion efficiency on interacting binary systems for different values of mass-ratio. As seen in Fig. 14, the [Rb/Fe] and [Zr/Fe] ratios derived for the targets HE 0457−1805 (B) and HE 2207−1746 (D) are consistent with the values observed in low-mass AGB stars. For the star HE 1255−2324 (C), the high [Rb/Fe] ratio is accompanied by similar level of [Zr/Fe], indicating large *s*-process efficiency in the processed material.

In Fig. 15, we have examined the [Zr/Fe] and [Nb/Fe] ratios. As demonstrated by Neyskens et al. (2015), under certain conditions, the [Zr/Fe] and [Nb/Fe] pair of abundance ratios observed in extrinsic

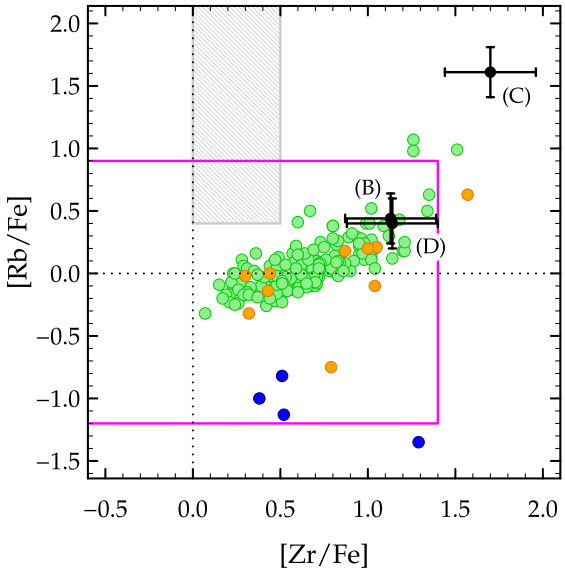

Figure 14. [Rb/Fe] *versus* [Zr/Fe] plane showing the distribution of the program stars (black dots with error bars), HE 0457−1805 (B), HE 1255−2324 (C), and HE 2207−1746 (D), along with data available for barium stars. Symbols have the same meaning as in Fig. 13. The magenta box delimits the ranges of the [Rb/Fe] and [Zr/Fe] ratios observed for low-mass AGB stars of the Galaxy and the Magellanic Clouds, whereas the grey shaded area shows the ranges observed for intermediate-mass AGB stars (van Raai et al. 2012).

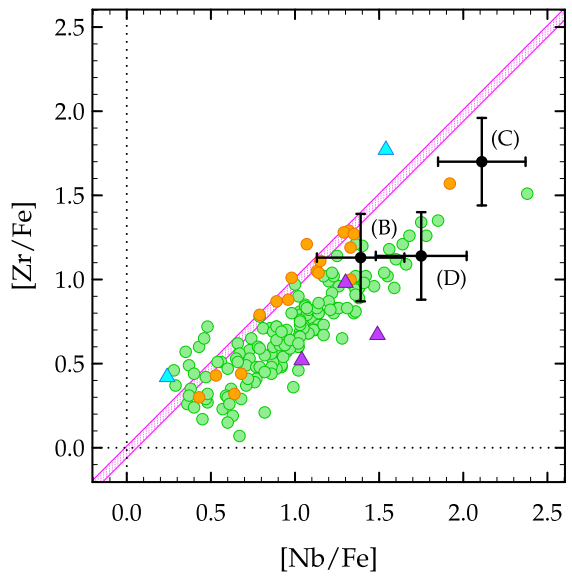

Figure 15. [Zr/Fe] *versus* [Nb/Fe] plane showing the distribution of the program stars (black dots with error bars), HE 0457−1805 (B), HE 1255−2324 (C), and HE 2207−1746 (D), along with data available for barium stars and CEMP stars. Symbols have the same meaning as in Fig. 13. The magenta region in this plot represents the analytical prediction reported by Neyskens et al. (2015) for extrinsic stars.

stars can be used as a temperature diagnostic of the *s*-process that operated inside the former donor AGB star, thus constraining its main neutron source. This analytical approach is based on the fact that Nb has only one stable isotope, ^{93}Nb, created exclusively from the β-decay of the ^{93}Zr ($T_{1/2} = 1.53 \times 10^6$ years). From the end of the *s*-process to the end of mass transfer, all the ^{93}Zr received by the evolved secondary star had time to decay into ^{93}Nb. Therefore, the Zr/Nb ratio, currently observed in the extrinsic star, should be equal to the Zr/^{93}Zr ratio in the atmosphere of the former AGB star. Assuming local equilibrium, in which the product $\langle\sigma_i\rangle N$, where $\langle\sigma_i\rangle$ is the Maxwellian-averaged neutron-capture cross-section, remains constant along an isotopic chain, the Zr/^{93}Zr can be written in terms of the $\langle\sigma_i\rangle$ for the Zr isotopes. The neutron-capture cross-sections in turn are temperature dependent; therefore, the current Zr/Nb ratio is a thermometer of the *s*-process responsible for the observed pattern.

For the temperature range of the *s*-process operation, i.e. (1–3) $\times$ 10^8 K, corresponding to k_BT = 10–30 keV, the analytical prediction reported by Neyskens et al. (2015) defines a region in the [Zr/Fe] *versus* [Nb/Fe] plane, as shown in Fig. 15, where it is expected to find extrinsic stars. Later, from more refined nucleosynthesis predictions computed by the STAREVOL models, for [Fe/H] =−0.5, Karinkuzhi et al. (2018) found a close agreement with the analytical model of Neyskens et al. for low-mass (1–3 $M_\odot$) AGB stars. On the other hand, for more massive (>4 $M_\odot$) AGB stars, the model predictions computed by these authors deviate from the analytical approach.

Karinkuzhi et al. (2018) and Roriz et al. (2021b) applied the method of Neyskens et al. (2015) for their respective sample of barium stars. While the targets considered of Karinkuzhi et al. (orange dots) fall partially in the predicted magenta region in Fig. 15, the stars of Roriz et al. (green dots) are found systematically below the predicted region, on the Nb-rich side of the plane. In this study, we examined the positions of the program stars in the [Zr/Fe] and [Nb/Fe] plane; we note that the stars HE 0457−1805 (B), HE 1255−2324 (C), and HE 2207−1746 (D), for which we were able to derive the [Zr/Fe] and [Nb/Fe] ratios, behave a similar trend as found by Roriz et al. In particular, HE 1255−2324 (C) stands out from other objects, with [Zr/Fe] = 1.70 and [Nb/Fe] = 2.08. The observed excess in [Nb/Fe] relative to the production model of Neyskens et al., however, seems to indicate the presence of an extra contribution to ^{93}Nb. This may derived from, e.g. ^{93}Y, if all the branching points at $^{90,\,91,\,92}$Y may be open in conditions of relatively high neutron densities. For example, to open the branching point at ^{93}Y, with a half-life of 3.54 h, sustained neutron densities above 10^{12} cm^{-3} would be required. New detailed models are needed to investigate the production of Nb in AGB stars.

In addition to the *s*-enrichment observed in our targets, as we have discussed, these stars also show atmospheres with high levels of the *r*-elements, displaying [*r*/Fe] = 1.02, 1.13, 1.41, and 1.14, respectively, for BD+03°2688, HE 0457−1805, HE 1255−2324, and HE 2207−1746, where [*r*/Fe] is the averaged abundance of the *r*-process elements, computed from the Sm and Eu abundances. However, if we also consider the *r*-element erbium in the [*r*/Fe] ratios, we then found higher *r*-process means, with [*r*/Fe] = 1.41, 1.85, and 1.35, respectively, for HE 0457−1805, HE 1255−2324, and HE 2207−1746. For BD+03°2688, we were not able to derive its Er abundance. In Fig. 16, we plot the [*r*/Fe] ratios as a function of [Zr/Nb], and compare them with data for barium stars. As evidenced in Fig. 16, the program stars show high levels of the [*r*/Fe] ratios, reaching values on the top of those commonly observed in barium stars. For HE 1255−2324, we stress that this system presents a [*r*/Fe] ratio similar to that found in the barium star HD 100503 ([*r*/Fe] = 1.45), previously reported by Karinkuzhi et al. (2018), who labelled this object as a possible analogue of CEMP-*r*/*s* star. As we have mentioned, these stars lie close to the CEMP-*r*/*s* stars in the [La/Fe] *versus* [Eu/Fe] diagram (Fig. 13).

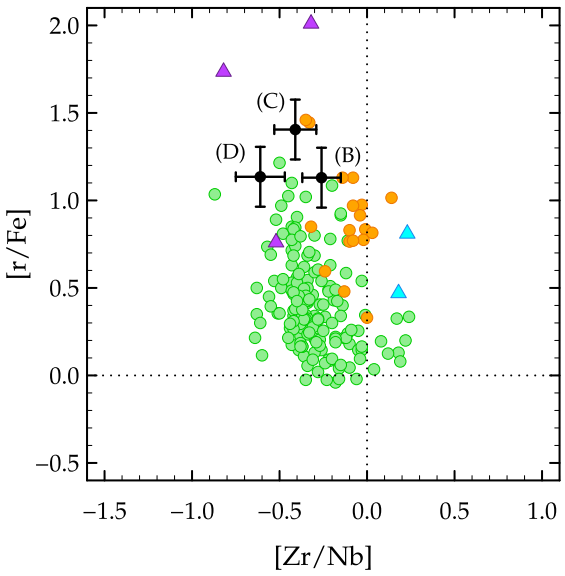

Figure 16. [*r*/Fe] *versus* [Zr/Nb] plane showing the distribution of the program stars (black dots with error bars), HE 0457−1805 (B), HE 1255−2324 (C), and HE 2207−1746 (D), where [*r*/Fe] =([Sm/Fe] + [Eu/Fe])/2 is the mean of the *r*-process elements. For comparison, we added to this plot data available for barium stars and CEMP stars. Symbols have the same meaning as in Figs 12 and 13.

5.4.1 Tungsten and thallium

Tungsten and thallium have a relatively high *s*-process contribution in the Solar system (see Table 7), and because they are located between the second and third *s*-process peaks, their abundances (relative to the peaks) during the *s*-process flux are mostly determined by their neutron-capture cross-sections. Once the flux reaches the second peak, the absolute amount of the elements beyond it that can be produced is a function of the neutron exposure, i.e. how many free neutrons are available. However, the distribution of such elements from Ba to Pb is controlled by the neutron capture cross-sections. In other words, if the final abundance of Pb is high or low, then the abundances of these elements are also high or low, as their relative fraction cannot vary strongly. This property was used by Lugaro et al. (2015) to analyse the abundance pattern observed in post-AGB stars (including elements such as W and Tl, and others in the same mass regions) and demonstrated that could not be a product of the *s*-process. Subsequently, Hampel et al. (2019) analysed these stars in the light of the intermediate *i*-process and obtained abundance patterns that could match them. This is because during the *i*-process the neutron-capture flux moves away from the valley of β stability, and it is possible in this case to enhance the abundances of e.g. W and Tl, without increasing that of Pb. In Fig. 17, we show a portion of the nuclide chart close to W and Tl, where we illustrate the *s*-process path throughout these species.

Because there are few data in literature for tungsten and lead, and no data for thallium, we do not plot them in Fig. 12. However, we can discuss the [W/hs], [Tl/hs] and [Pb/W], [Pb/Tl] ratios of our stars as compared to nucleosynthesis models in the next section.

5.5 Comparison to nucleosynthesis models

In Fig. 18, panels (a), (b), and (c), we plot different abundance ratios, and compare them with predictions from two different sets of the *s*-process models, in order to probe the physical conditions that would originate the *s*-pattern observed in the program stars. We also added in this figure data for barium stars, CH stars, and post-AGB stars, when available. The Monash models are provided by Fishlock et al. (2014), Karakas & Lugaro (2016), and Karakas et al. (2018), with the standard choice of the partial mixing zone leading to the formation of the ^{13}C pocket. The FRUITY (FUll-Network Repository of Updated Isotopic Tables & Yields) nucleosynthesis models (Cristallo et al. 2011) are provided online by the FRUITY

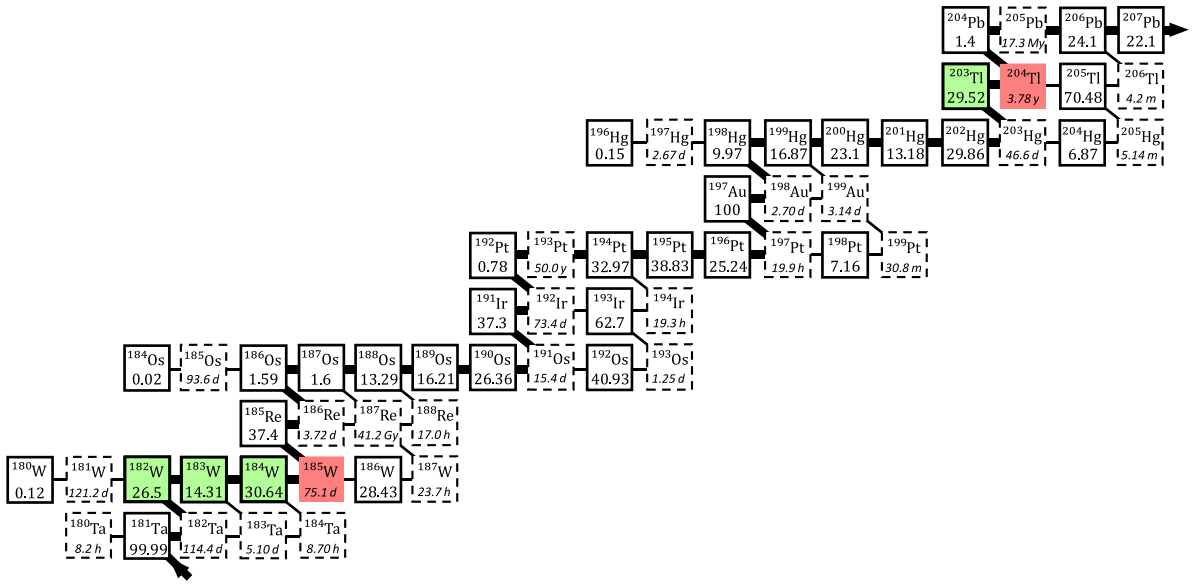

Figure 17. A portion of the nuclide chart showing the main (bold lines) and secondaries (thin lines) *s*-process paths from Ta to Pb. For unstable isotopes (dashed line boxes), we show their half-lives in italic, whereas for the stable ones (bold line boxes), we show their per cent abundances. Data for this figure were taken from Dillmann et al. (2006). The branching points at ^{185}W and ^{204}Tl are identified in red boxes, while the green boxes are the stable isotopes of the W and Tl nuclide along the main *s*-process path.

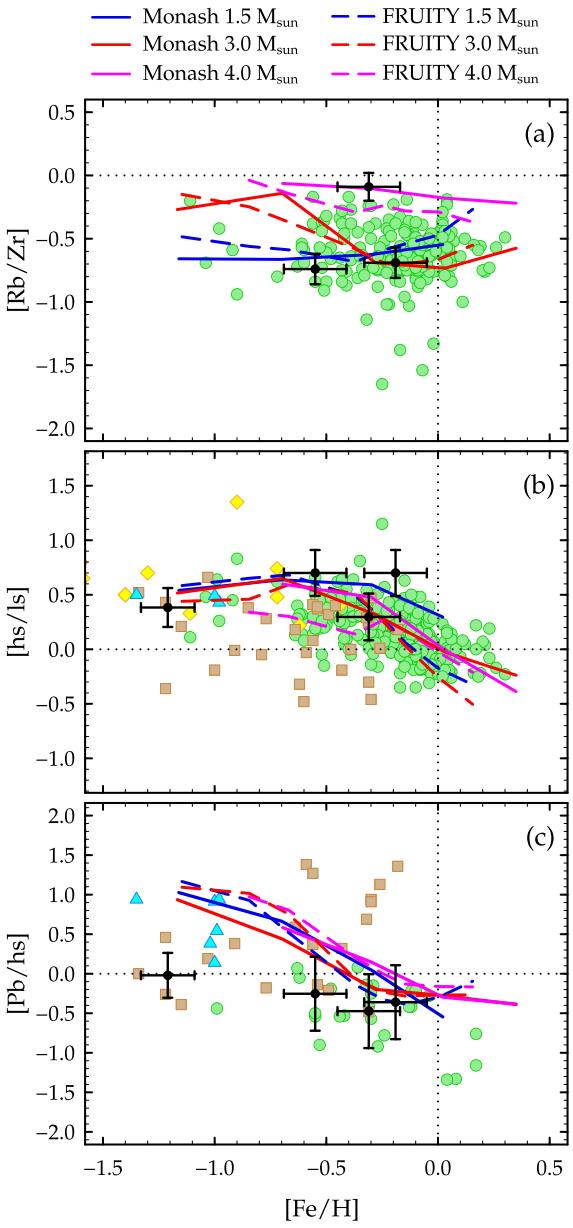

Figure 18. Comparison between the observed [Rb/Zr] (panel a), [hs/ls] (panel b), and [Pb/hs] (panel c) ratios with theoretical predictions from the Monash and FRUITY *s*-process models for low-mass AGB stars. Symbols have the same meaning as in Fig. 12.

data base,[3] not including rotation, and with the standard choice of the ^{13}C pocket. However, because the models do not account the mass transfer and the further dilution of the AGB material deposited in the convective atmosphere of the observed star, we cannot directly compare the models predictions with the data for [X/Fe]. Instead, we should consider only ratios that cancel the dilution effects.

In Fig. 18 (a), we plot the [Rb/Zr] ratios *versus* [Fe/H]. As we have argued in the previous section, rubidium is a key element for neutron density diagnostic of the *s*-process, thanks to the branch points at ^{85}Kr and ^{86}Rb along the *s*-process path. In fact, the abundance ratios between Rb and its neighboring elements Sr and Zr, [Rb/Sr, Zr], can be also used as a probe to constraint the main neutron source of the *s*-process, and consequently the mass of the polluting AGB star. In the light of the *s*-process models, it is expected [Rb/Sr, Zr] <0 for low-mass AGB stars, in which ^{13}C is the main neutron source of the *s*-process, and [Rb/Sr, Zr] >0 for more massive AGB stars, in which ^{22}Ne becomes the main neutron source. This fact has been used for many authors to constrain the AGB mass (e.g. Lambert et al. 1995; Abia et al. 2001; García-Hernández et al. 2006, 2009; van Raai et al. 2012; Shejeelammal et al. 2020; Roriz et al. 2021a). For the stars HE 0457−1805, HE 1255−2324, and HE 2207−1746, we found [Rb/Zr] <0. For the star BD+03°2688, however, we were not able to compute its rubidium abundance, since the Rb line was too weak to be detected in its spectrum.

In Fig. 18 (b), we investigate the behaviour of the *s*-process peaks, which occur close to the elements with magic number of neutrons; these elements tend to accumulate due to their low neutron-capture cross-section. The light *s*-elements (Sr, Y, and Zr) form the first peak, the heavy *s*-elements (La, Ce, and Nd) form the second peak, and the third peak occurs close to Pb. The index [hs/ls] = [hs/Fe]−[ls/Fe], where [hs/Fe] and [ls/Fe] are, respectively, the means of the heavy and light *s*-elements, is commonly used as a probe of the *s*-process efficiency (Busso et al. 2001). From panel (b), we can see that the observed data are in good agreement with the models predictions. The stars HE 0457−1805 and HE 2207−1746 show [hs/ls] ratios in the top range of the values commonly observed in barium stars in the same range of metallicity, indicating higher neutron exposures where the *s*-rich material of these stars was previously processed. In panel (c), we consider the [Pb/hs] ratios. The stars HE 0457−1805, HE 1255−2324, and HE 2207−1746 show typical values found in barium stars, which are slightly lower than the models. For metallicities near to BD+03°2688, the models predict [Pb/hs] ∼1, because more neutrons per iron seed are available for the *s*-process. This is much larger than the observed in this object (i.e. [Pb/hs] ∼0). This is similar to the case of post-AGB stars of similar metallicity showing Pb abundances much lower than expected by the models (Lugaro et al. 2015) and probably due to the operation of the *i*-process (Hampel et al. 2019). Taken together, since we observe [Pb/hs] $\lesssim$ 0 for the target stars, we can conclude that the *s*-process was not efficient in producing Pb. This is predicted by the AGB models for metallicities around solar, which also show [Pb/hs] $\lesssim$ 0.

We can infer more information from the W and Tl abundances and their relationship with the hs elements and with Pb (Fig. 19). Relative to each other and to the second peak elements, the models show small variations, because in the *s*-process W and Tl follows the hs elements according to their neutron-capture cross-sections, and therefore their ratios are typically solar. On the other hand, the Pb abundance increases, relative to W and Tl, with decreasing metallicity. The three stars for which W and Tl could be observed do not significantly deviate from the model predictions, except for HE 0457−1805 (B) for which Tl may have been slightly under estimated by the observations. It will be interesting to derive W and Tl for BD+03°2688 to investigate if the lower [Pb/hs] seen in this star to be lower than the model prediction is accompanied by an underabundance of these two elements as well.

6 CONCLUSIONS

Based on high-resolution optical spectroscopic data, we reported the first detailed chemical abundance analysis for a sample of

[3]Available at: http://fruity.oa-teramo.inaf.it/.

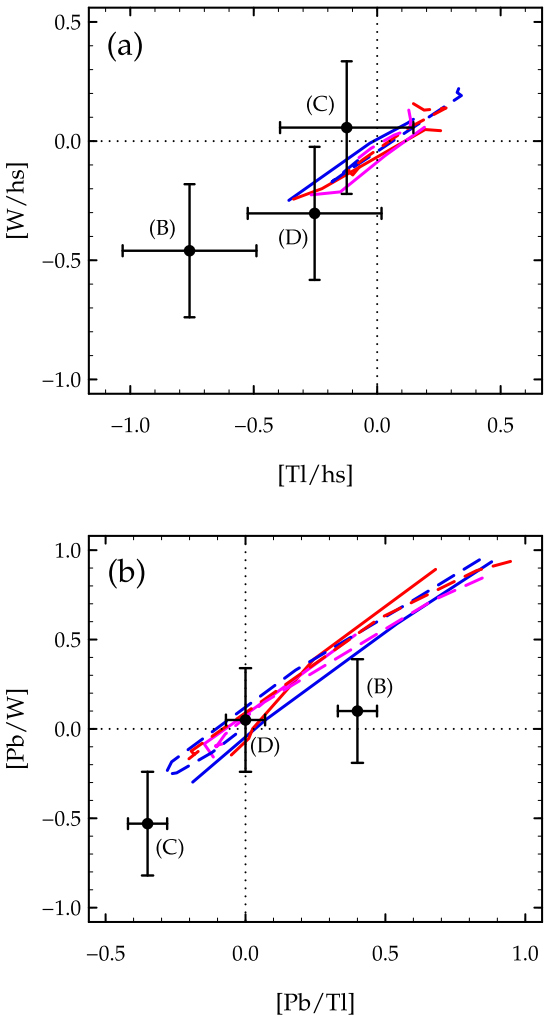

Figure 19. Different abundance ratios among the hs index and the heavy elements W, Tl, and Pb derived for the program stars (black dots with error bars) HE 0457−1805 (B), HE 1255−2324 (C), and HE 2207−1746 (D). The observed data set are compared with the same set of the *s*-process nucleosynthesis models showed in Fig. 18.

four new chemically peculiar stars, BD+03°2688, HE 0457−1805, HE 1255−2324, and HE 2207−1746, for which we have derived atmospheric parameters and abundances for several chemical elements. Although these targets show in their atmospheres high levels of the *s*-process elements, with [*s*/Fe] >1.0, they are not luminous enough to be intrinsic AGB stars and experience internal nucleosyntheis of the *s*-process; in fact, these systems are first-ascent giant branch stars.

The abundance ratios obtained in this work were compared with data for barium stars, CH stars, post-AGB stars and field giant stars, evidencing the *s*-rich nature of the program stars. HE 0457−1805 and HE 1255−2324 are binary stars; therefore, we can attribute their chemical peculiarities to mass transfer mechanism. We have identified HE 0457−1805 as a new barium star, since its C/O ratio is lesser the unity (C/O = 0.76), while HE 1255−2324 is a new CH star (C/O = 1.55). BD+03°2688 and HE 2207−1746 are probably CH stars, with C/O = 1.23 and 1.45, respectively, although this conclusion awaits an extensive radial-velocity monitoring.

Further to the *s*-enhancement ([*s*/Fe] =1.77) observed in HE 1255−2324, this star also shows a large amount of the *r*-elements Sm and Eu, with [*r*/Fe] = 1.41, at [Fe/H] = −0.31. So far, the first object reported in literature sharing similar characteristics was the barium star HD 100503 ([Fe/H] = −0.72), analysed by Karinkuzhi et al. (2018), who argued that HD 100503 would be an analogue of CEMP-*r*/*s* stars. Therefore, we conclude that the new CH star HE 1255−2324 is a higher metallicity analogue of CEMP-*r*/*s* stars.

We compare the observed data for the *s*-elements with predictions from the Monash and FRUITY *s*-process models. We derived for the sample stars [Rb/Zr] <0; from the nucleosynthesis models, this ratio is expected to be negative for low-mass (1–4 $M_{\odot}$) AGB stars. Furthermore, the low-mass AGB nucleosynthesis models are able to reproduce in good agreement the observed [hs/ls] ratios. On the other hand, models predict somewhat higher [Pb/hs] ratios than the observed for the targets of this study and other barium stars collected from literature; at the lowest metallicity of BD+03°2688 ([Fe/H] = −1.21), this mismatch is the most evident. Tungsten and thallium abundances were derived for the first time in the target systems of this study, and the new abundance ratios are in general agreement with the *s*-process nucleosynthesis models.

ACKNOWLEDGEMENTS

MPR acknowledges Conselho Nacional de Desenvolvimento Científico e Tecnológico (CNPq) for the postdoctoral fellowship No 313426/2022-8. ML acknowledges the support of the Hungarian National Research, Development and Innovation Office (NKFI), grant KH_18 130405. NAD acknowledges Fundação de Amparo à Pesquisa do Estado do Rio de Janeiro (FAPERJ), Rio de Janeiro, Brazil, for grant E-26/203.847/2022. CS thanks the U.S. National Science Foundation for support under grant AST 1616040. The authors thank the anonymous referee for the comments that helped to improve the manuscript. This work is based on the observations made with the 2.2 m telescope at the European Southern Observatory (La Silla, Chile) under the agreement with Observatório Nacional and under agreement between Observatório Nacional and Max-Planck Institute für Astronomie. This research has made use of NASA's Astrophysics Data System Bibliographic Services, and the SIMBAD (Wenger et al. 2000), VALD (Ryabchikova et al. 2015), and NIST (Kramida et al. 2021) data bases. This research has made also use of the NASA/IPAC Infrared Science Archive (IRSA 2022), which is funded by the National Aeronautics and Space Administration and operated by the California Institute of Technology.

DATA AVAILABILITY

The data underlying this article will be shared on reasonable request to the corresponding author.

REFERENCES

Abia C., Busso M., Gallino R., Domínguez I., Straniero O., Isern J., 2001, ApJ, 559, 1117
Abia C., de Laverny P., Korotin S., Asensio Ramos A., Recio-Blanco A., Prantzos N., 2021, A&A, 648, A107
Allen D. M., Barbuy B., 2006, A&A, 454, 895
Allen D. M., Porto de Mello G. F., 2007, A&A, 474, 221
Allende Prieto C., Lambert D. L., Asplund M., 2001, ApJ, 556, L63
Alonso A., Arribas S., Martínez-Roger C., 1999, A&AS, 140, 261
Alves-Brito A., Meléndez J., Asplund M., Ramírez I., Yong D., 2010, A&A, 513, A35
Antipova L. I., Boyarchuk A. A., Pakhomov Y. V., Panchuk V. E., 2004, Astron. Rep., 48, 597
Aoki W., Beers T. C., Christlieb N., Norris J. E., Ryan S. G., Tsangarides S., 2007, ApJ, 655, 492

Arentsen A. et al., 2019, A&A, 627, A138
Arlandini C., Käppeler F., Wisshak K., Gallino R., Lugaro M., Busso M., Straniero O., 1999, ApJ, 525, 886
Bailer-Jones C. A. L., Rybizki J., Fouesneau M., Mantelet G., Andrae R., 2018, AJ, 156, 58
Barbuy B., 1988, A&A, 191, 121
Barbuy B., Erdelyi-Mendes M., 1989, A&A, 214, 239
Barbuy B., Jorissen A., Rossi S. C. F., Arnould M., 1992, A&A, 262, 216
Beers T. C., Christlieb N., 2005, ARA&A, 43, 531
Bessell M. S., Castelli F., Plez B., 1998, A&A, 333, 231
Bidelman W. P., 1957, PASP, 69, 573
Bidelman W. P., Keenan P. C., 1951, ApJ, 114, 473
Bisterzo S., Travaglio C., Gallino R., Wiescher M., Käppeler F., 2014, ApJ, 787, 10
Boothroyd A. I., Sackmann I.-J., 1999, ApJ, 510, 232
Burris D. L., Pilachowski C. A., Armandroff T. E., Sneden C., Cowan J. J., Roe H., 2000, ApJ, 544, 302
Busso M., Gallino R., Lambert D. L., Travaglio C., Smith V. V., 2001, ApJ, 557, 802
Carretta E., Gratton R. G., Sneden C., 2000, A&A, 356, 238
Carretta E., Bragaglia A., Gratton R. G., 2007, A&A, 473, 129
Charbonnel C., 1994, A&A, 282, 811
Charbonnel C., 1995, ApJ, 453, L41
Chen B., Vergely J. L., Valette B., Carraro G., 1998, A&A, 336, 137
Chen Y. Q., Zhao G., Nissen P. E., Bai G. S., Qiu H. M., 2003, ApJ, 591, 925
Chen Z., Ivanova N., Carroll-Nellenback J., 2020, ApJ, 892, 110
Christlieb N., Green P. J., Wisotzki L., Reimers D., 2001, A&A, 375, 366
Cowan J. J., Rose W. K., 1977, ApJ, 212, 149
Cowan J. J., Sneden C., Lawler J. E., Aprahamian A., Wiescher M., Langanke K., Martínez-Pinedo G., Thielemann F.-K., 2021, Rev. Mod. Phys., 93, 015002
Cristallo S. et al., 2011, ApJS, 197, 17
Cseh B. et al., 2018, A&A, 620, A146
Cseh B. et al., 2022, A&A, 660, A128
de Castro D. B., Pereira C. B., Roig F., Jilinski E., Drake N. A., Chavero C., Sales Silva J. V., 2016, MNRAS, 459, 4299
De Smedt K., Van Winckel H., Karakas A. I., Siess L., Goriely S., Wood P. R., 2012, A&A, 541, A67
De Smedt K., Van Winckel H., Kamath D., Wood P. R., 2015, A&A, 583, A56
De Smedt K., Van Winckel H., Kamath D., Siess L., Goriely S., Karakas A. I., Manick R., 2016, A&A, 587, A6
de Strobel G. C., Spite M., 1988, Proc. IAU Symp. 132, The Impact of Very High S/N Spectroscopy on Stellar Physics. Springer Science & Business Media, France
Den Hartog E. A., Lawler J. E., Sneden C., Cowan J. J., 2003, ApJS, 148, 543
Denisenkov P. A., Ivanov V. V., 1987, Sov. Astron. Lett., 13, 214
Depagne E. et al., 2002, A&A, 390, 187
Dillmann I., Heil M., Käppeler F., Plag R., Rauscher T., Thielemann F. K., 2006, in Woehr A., Aprahamian A., eds, AIP Conf. Ser. Vol. 819, Capture Gamma-Ray Spectroscopy and Related Topics. Am. Inst. Phys., New York, p. 123
Drake N. A., Pereira C. B., 2008, AJ, 135, 1070
Drake J. J., Smith G., 1991, MNRAS, 250, 89
Edvardsson B., Andersen J., Gustafsson B., Lambert D. L., Nissen P. E., Tomkin J., 1993, A&A, 500, 391
Fishlock C. K., Karakas A. I., Lugaro M., Yong D., 2014, ApJ, 797, 44
For B.-Q., Sneden C., 2010, AJ, 140, 1694
Forsberg R., Jönsson H., Ryde N., Matteucci F., 2019, A&A, 631, A113
Gałan C., Mikołajewska J., Hinkle K. H., Joyce R. R., 2016, MNRAS, 455, 1282
Gałan C., Mikołajewska J., Hinkle K. H., Joyce R. R., 2017, MNRAS, 466, 2194
García-Hernández D. A., García-Lario P., Plez B., D'Antona F., Manchado A., Trigo-Rodríguez J. M., 2006, Science, 314, 1751
García-Hernández D. A. et al., 2009, ApJ, 705, L31
Girardi L., Bressan A., Bertelli G., Chiosi C., 2000, A&AS, 141, 371
Goswami A., 2005, MNRAS, 359, 531
Goswami A., Aoki W., Karinkuzhi D., 2016, MNRAS, 455, 402
Goswami P. P., Rathour R. S., Goswami A., 2021, A&A, 649, A49
Gratton R. G., Ortolani S., 1986, A&A, 169, 201
Gratton R. G., Sneden C., 1988, A&A, 204, 193
Gratton R. G., Sneden C., 1994, A&A, 287, 927
Gratton R. G., Sneden C., Carretta E., Bragaglia A., 2000, A&A, 354, 169
Grevesse N., Sauval A. J., 1998, Space Sci. Rev., 85, 161
Hampel M., Stancliffe R. J., Lugaro M., Meyer B. S., 2016, ApJ, 831, 171
Hampel M., Karakas A. I., Stancliffe R. J., Meyer B. S., Lugaro M., 2019, ApJ, 887, 11
Han Z., Eggleton P. P., Podsiadlowski P., Tout C. A., 1995, MNRAS, 277, 1443
Hansen C. J., Andersen A. C., Christlieb N., 2014, A&A, 568, A47
Hansen T. T., Andersen J., Nordström B., Beers T. C., Placco V. M., Yoon J., Buchhave L. A., 2016, A&A, 588, A3
Hansen C. J., Hansen T. T., Koch A., Beers T. C., Nordström B., Placco V. M., Andersen J., 2019, A&A, 623, A128
Hartwick F. D. A., Cowley A. P., 1985, AJ, 90, 2244
Iben Icko J., 1964, ApJ, 140, 1631
Iben Icko J., 1965, ApJ, 142, 1447
Iben Icko J., 1967, ApJ, 147, 624
IRSA, 2022, Galactic Dust Reddening and Extinction. IPAC, Caltech
Ishigaki M. N., Tominaga N., Kobayashi C., Nomoto K., 2018, ApJ, 857, 46
Johnson J. A., 2002, ApJS, 139, 219
Jorissen A., Van Eck S., Mayor M., Udry S., 1998, A&A, 332, 877
Jorissen A., Začs L., Udry S., Lindgren H., Musaev F. A., 2005, A&A, 441, 1135
Jorissen A. et al., 2016, A&A, 586, A158
Jorissen A., Boffin H. M. J., Karinkuzhi D., Van Eck S., Escorza A., Shetye S., Van Winckel H., 2019, A&A, 626, A127
Junqueira S., Pereira C. B., 2001, AJ, 122, 360
Käppeler F., Gallino R., Bisterzo S., Aoki W., 2011, Rev. Mod. Phys., 83, 157
Karakas A. I., Lattanzio J. C., 2014, Publ. Astron. Soc. Aust., 31, e030
Karakas A. I., Lugaro M., 2016, ApJ, 825, 26
Karakas A. I., Lugaro M., Carlos M., Cseh B., Kamath D., García-Hernández D. A., 2018, MNRAS, 477, 421
Karinkuzhi D., Goswami A., 2014, MNRAS, 440, 1095
Karinkuzhi D. et al., 2018, A&A, 618, A32
Karinkuzhi D., Van Eck S., Goriely S., Siess L., Jorissen A., Merle T., Escorza A., Masseron T., 2021, A&A, 645, A61
Kaufer A., Pasquini L., 1998, in D'Odorico S., ed., Proc. SPIE Conf. Ser. Vol. 3355, Optical Astronomical Instrumentation. SPIE, Bellingham, p. 844
Kaufer A., Stahl O., Tubbesing S., Nørregaard P., Avila G., Francois P., Pasquini L., Pizzella A., 1999, The Messenger, 95, 8
Keenan P. C., 1942, ApJ, 96, 101
Kennedy C. R. et al., 2011, AJ, 141, 102
Koch A., Reichert M., Hansen C. J., Hampel M., Stancliffe R. J., Karakas A., Arcones A., 2019, A&A, 622, A159
Kraft R. P., Sneden C., Langer G. E., Prosser C. F., 1992, AJ, 104, 645
Kramida A., Yu. Ralchenko Reader J., NIST ASD Team, 2021, NIST Atomic Spectra Database (ver. 5.9). [Online]. Available: https://physics.nist.gov/asd
Kunder A. et al., 2017, AJ, 153, 75
Kurucz R., 1993, ATLAS9 Stellar Atmosphere Programs and 2 km/s Grid. Kurucz CD-ROM No. 13., Smithsonian Astrophysical Observatory, Cambridge, p. 13
Lambert D. L., 1981, in Iben I. J., Renzini A., eds, Astrophysics and Space Science Library, Vol. 88, Physical Processes in Red Giants. Springer-Verlag, Berlin, p. 115
Lambert D. L., Mallia E. A., Smith G., 1972, Sol. Phys., 26, 250
Lambert D. L., Gustafsson B., Eriksson K., Hinkle K. H., 1986, ApJS, 62, 373
Lambert D. L., Smith V. V., Busso M., Gallino R., Straniero O., 1995, ApJ, 450, 302
Lambert D. L., Heath J. E., Lemke M., Drake J., 1996, ApJS, 103, 183
Lattanzio J. C., 1986, ApJ, 311, 708
Lawler J. E., Bonvallet G., Sneden C., 2001a, ApJ, 556, 452

Lawler J. E., Wickliffe M. E., den Hartog E. A., Sneden C., 2001b, ApJ, 563, 1075
Lawler J. E., Den Hartog E. A., Sneden C., Cowan J. J., 2006, ApJS, 162, 227
Lawler J. E., Sneden C., Cowan J. J., Ivans I. I., Den Hartog E. A., 2009, ApJS, 182, 51
Liu Z.-W., Stancliffe R. J., Abate C., Matrozis E., 2017, ApJ, 846, 117
Lucatello S., Tsangarides S., Beers T. C., Carretta E., Gratton R. G., Ryan S. G., 2005, ApJ, 625, 825
Luck R. E., Bond H. E., 1991, ApJS, 77, 515
Luck R. E., Heiter U., 2007, AJ, 133, 2464
Lugaro M., Campbell S. W., Van Winckel H., De Smedt K., Karakas A. I., Käppeler F., 2015, A&A, 583, A77
McClure R. D., 1984, ApJ, 280, L31
McClure R. D., Woodsworth A. W., 1990, ApJ, 352, 709
McClure R. D., Fletcher J. M., Nemec J. M., 1980, ApJ, 238, L35
McDonald I., Zijlstra A. A., Watson R. A., 2017, MNRAS, 471, 770
McWilliam A., Rich R. M., 1994, ApJS, 91, 749
McWilliam A., Preston G. W., Sneden C., Searle L., 1995, AJ, 109, 2757
Masseron T., Johnson J. A., Plez B., van Eck S., Primas F., Goriely S., Jorissen A., 2010, A&A, 509, A93
Meléndez J., Barbuy B., 2009, A&A, 497, 611
Mishenina T. V., Kovtyukh V. V., 2001, A&A, 370, 951
Mishenina T. V., Bienaymé O., Gorbaneva T. I., Charbonnel C., Soubiran C., Korotin S. A., Kovtyukh V. V., 2006, A&A, 456, 1109
Mishenina T. V., Gorbaneva T. I., Bienaymé O., Soubiran C., Kovtyukh V. V., Orlova L. F., 2007, Astron. Rep., 51, 382
Mowlavi N., 1999, A&A, 344, 617
Munari U. et al., 2014, AJ, 148, 81
Neyskens P., van Eck S., Jorissen A., Goriely S., Siess L., Plez B., 2015, Nature, 517, 174
Pereira C. B., Drake N. A., 2009, A&A, 496, 791
Pereira C. B., Sales Silva J. V., Chavero C., Roig F., Jilinski E., 2011, A&A, 533, A51
Pereira C. B., Jilinski E., Drake N. A., de Castro D. B., Ortega V. G., Chavero C., Roig F., 2012, A&A, 543, A58
Pereira C. B., Holanda N., Drake N. A., Roig F., 2019a, AJ, 157, 70
Pereira C. B., Drake N. A., Roig F., 2019b, MNRAS, 488, 482
Pourbaix D. et al., 2004, A&A, 424, 727
Preston G. W., Sneden C., 2001, AJ, 122, 1545
Purandardas M., Goswami A., Goswami P. P., Shejeelammal J., Masseron T., 2019, MNRAS, 486, 3266
Reddy B. E., Bakker E. J., Hrivnak B. J., 1999, ApJ, 524, 831
Reddy B. E., Tomkin J., Lambert D. L., Allende Prieto C., 2003, MNRAS, 340, 304
Reyniers M., Van Winckel H., Gallino R., Straniero O., 2004, A&A, 417, 269
Roederer I. U., Karakas A. I., Pignatari M., Herwig F., 2016, ApJ, 821, 37
Roriz M., Pereira C. B., Drake N. A., Roig F., Silva J. V. S., 2017, MNRAS, 472, 350
Roriz M. P., Lugaro M., Pereira C. B., Drake N. A., Junqueira S., Sneden C., 2021a, MNRAS, 501, 5834
Roriz M. P., Lugaro M., Pereira C. B., Sneden C., Junqueira S., Karakas A. I., Drake N. A., 2021b, MNRAS, 507, 1956
Ryabchikova T., Piskunov N., Kurucz R. L., Stempels H. C., Heiter U., Pakhomov Y., Barklem P. S., 2015, A Major Upgrade of the VALD Database. Available: http://vald.astro.uu.se/
Santrich O. J. K., Pereira C. B., Drake N. A., 2013, A&A, 554, A2
Shejeelammal J., Goswami A., Goswami P. P., Rathour R. S., Masseron T., 2020, MNRAS, 492, 3708
Shetrone M. D., 1996, AJ, 112, 1517
Simmerer J., Sneden C., Cowan J. J., Collier J., Woolf V. M., Lawler J. E., 2004, ApJ, 617, 1091
Smiljanic R., Gauderon R., North P., Barbuy B., Charbonnel C., Mowlavi N., 2009, A&A, 502, 267
Smith V. V., 1984, A&A, 132, 326
Smith V. V., Lambert D. L., 1985, ApJ, 294, 326
Smith G., Edvardsson B., Frisk U., 1986, A&A, 165, 126
Smith V. V., Cunha K., Jorissen A., Boffin H. M. J., 1996, A&A, 315, 179
Sneden C. A., 1973, PhD thesis, The University of Texas at Austin
Sneden C., 1991, in Michaud G., Tutukov A. V., eds, Proc. IAU Symp. Vol. 145, Evolution of Stars: the Photospheric Abundance Connection. Cambridge Univ. Press, Cambridge, p. 235
Sneden C., Kraft R. P., Prosser C. F., Langer G. E., 1991, AJ, 102, 2001
Sneden C., McWilliam A., Preston G. W., Cowan J. J., Burris D. L., Armosky B. J., 1996, ApJ, 467, 819
Spite M. et al., 2005, A&A, 430, 655
Spite M. et al., 2006, A&A, 455, 291
Spite M., Caffau E., Bonifacio P., Spite F., Ludwig H.-G., Plez B., Christlieb N., 2013, A&A, 552, A107
Stancliffe R. J., 2021, MNRAS, 505, 5554
Starkenburg E., Shetrone M. D., McConnachie A. W., Venn K. A., 2014, MNRAS, 441, 1217
Stevens D. J., Stassun K. G., Gaudi B. S., 2017, AJ, 154, 259
Szigeti L. et al., 2018, MNRAS, 474, 4810
Takeda Y., 2021, Astron. Nachr., 342, 515
Takeda Y., Sato B., Murata D., 2008, PASJ, 60, 781
Takeda Y., Omiya M., Harakawa H., Sato B., 2019, PASJ, 71, 119
Tautvaišienė B., Edvardsson B., Puzeras E., Barisevičius G., Ilyin I., 2010, MNRAS, 409, 1213
Tautvaišienė G., Barisevičius G., Chorniy Y., Ilyin I., Puzeras E., 2013, MNRAS, 430, 621
Tautvaišienė G. et al., 2015, A&A, 573, A55
Tautvaišienė G., Drazdauskas A., Bragaglia A., Randich S.,Ženovienė R., 2016, A&A, 595, A16
Timmes F. X., Woosley S. E., Weaver T. A., 1995, ApJS, 98, 617
Tomkin J., Lambert D. L., 1984, ApJ, 279, 220
Tomkin J., Lambert D. L., 1999, ApJ, 523, 234
van Aarle E., Van Winckel H., De Smedt K., Kamath D., Wood P. R., 2013, A&A, 554, A106
Van Eck S., Jorissen A., 1999, A&A, 345, 127
Van Eck S., Goriely S., Jorissen A., Plez B., 2003, A&A, 404, 291
van Raai M. A., Lugaro M., Karakas A. I., García-Hernández D. A., Yong D., 2012, A&A, 540, A44
Van Winckel H., Reyniers M., 2000, A&A, 354, 135
Vanture A. D., 1992a, AJ, 103, 2035
Vanture A. D., 1992b, AJ, 104, 1986
Vanture A. D., 1992c, AJ, 104, 1997
Vanture A. D., Wallerstein G., 1999, PASP, 111, 84
Vassiliadis E., Wood P. R., 1993, ApJ, 413, 641
Veklich A. N., Lebid A. V., Tmenova T. A., 2015, J. Astrophys. Astron., 36, 589
Wahlgren G. M., Dolk L., Kalus G., Johansson S., Litzén U., Leckrone D. S., 2000, ApJ, 539, 908
Wenger M. et al., 2000, A&AS, 143, 9
Wiese W. L., Smith M. W., Miles B. M., 1969, Atomic Transition Probabilities. Vol. 2: Sodium Through Calcium. A Critical Data Compilation. National Bureau of Standards, Washington, D.C.
Woosley S. E., Weaver T. A., 1995, ApJS, 101, 181
Zhang L., Ishigaki M., Aoki W., Zhao G., Chiba M., 2009, ApJ, 706, 1095

APPENDIX A: OBSERVED ATOMIC LINES IN THE SPECTRA OF THE PROGRAM STARS

Table A1. Equivalent width measurements of the Fe I and Fe II lines considered in this study.

Element	Wavelength (Å)	χ (eV)	log gf	Equivalent widths (mÅ)			
				BD+03°2688	HE 0457-1805	HE 1255−2324	HE 2207−1746
Fe I	5198.71	2.22	−2.14	110	–	131	128
	5242.49	3.63	−0.97	82	114	–	100
	5250.21	0.12	−4.92	118	–	–	–
	5253.03	2.28	−3.79	26	–	–	–
	5281.79	3.04	−0.83	123	–	–	–
	5288.52	3.69	−1.51	44	90	74	79
	5307.36	1.61	−2.97	103	–	120	121
	5322.04	2.28	−2.84	74	–	93	89
	5364.87	4.45	+0.23	88	–	–	–
	5367.47	4.42	+0.43	96	–	–	124
	5369.96	4.37	+0.54	104	–	–	–
	5373.71	4.47	−0.71	39	–	72	–
	5389.48	4.42	−0.25	75	126	118	98
	5393.17	3.24	−0.72	119	–	–	–
	5400.50	4.37	−0.10	89	–	–	–
	5410.91	4.47	+0.40	91	138	–	–
	5417.03	4.42	−1.53	–	–	–	–
	5445.04	4.39	+0.04	90	–	–	–
	5522.45	4.21	−1.40	–	–	–	–
	5560.21	4.43	−1.04	34	67	–	–
	5567.39	2.61	−2.56	87	–	–	–
	5624.02	4.39	−1.33	–	60	–	–
	5635.82	4.26	−1.74	–	–	53	–
	5686.53	4.55	−0.45	69	–	–	94
	5691.50	4.30	−1.37	36	–	–	63
	5705.47	4.30	−1.36	25	56	50	42
	5717.83	4.28	−0.97	47	–	–	75
	5731.76	4.26	−1.15	54	–	–	–
	5762.99	4.21	−0.41	81	–	–	104
	5791.02	3.21	−2.27	63	–	–	–
	5806.73	4.61	−0.90	29	74	67	57
	5814.81	4.28	−1.82	16	–	–	44
	5852.22	4.55	−1.18	–	73	53	46
	5883.82	3.96	−1.21	51	–	89	–
	5916.25	2.45	−2.99	61	–	84	94
	6024.06	4.55	−0.06	80	–	–	–
	6027.05	4.08	−1.09	48	99	81	82
	6056.01	4.73	−0.40	43	75	78	67
	6065.48	2.61	−1.53	129	–	–	–
	6079.01	4.65	−0.97	24	62	57	44
	6082.71	2.22	−3.58	41	–	–	61
	6093.64	4.61	−1.35	–	–	37	–
	6096.66	3.98	−1.78	21	62	–	41
	6136.61	2.45	−1.40	138	–	–	–
	6137.69	2.59	−1.40	135	–	–	–
	6151.62	2.18	−3.29	59	104	84	81
	6165.36	4.14	−1.47	30	80	63	56
	6173.34	2.22	−2.88	86	–	–	–
	6187.99	3.94	−1.57	35	90	–	–
	6191.56	2.43	−1.42	143	–	–	–
	6200.31	2.60	−2.44	75	–	–	105
	6213.43	2.22	−2.48	99	–	–	131
	6252.56	2.40	−1.72	131	–	–	–
	6254.26	2.28	−2.44	116	–	–	–
	6265.13	2.18	−2.55	109	–	–	–
	6311.50	2.83	−3.23	–	–	–	38
	6322.69	2.59	−2.43	80	–	121	109
	6380.74	4.19	−1.32	47	–	–	–
	6392.54	2.28	−4.03	–	70	50	49
	6393.60	2.43	−1.43	142	–	–	–
	6411.65	3.65	−0.66	104	–	–	129
	6419.95	4.73	−0.09	61	–	115	–
	6421.35	2.28	−2.01	128	–	–	–

Table A1 – *continued*

Element	Wavelength (Å)	χ (eV)	log gf	Equivalent widths (mÅ) BD+03°2688	HE 0457-1805	HE 1255−2324	HE 2207−1746
	6430.85	2.18	−2.01	137	–	–	–
	6518.37	2.83	−2.30	–	106	93	–
	6551.68	0.99	−5.79	–	–	–	40
	6574.23	0.99	−5.02	–	–	96	92
	6592.91	2.72	−1.47	117	–	137	–
	6593.87	2.44	−2.42	95	–	125	–
	6597.56	4.79	−0.92	23	–	46	48
	6608.03	2.28	−4.03	–	62	43	32
	6609.11	2.56	−2.69	73	–	103	93
	6704.48	4.22	−2.66	–	25	–	–
	6739.52	1.56	−4.95	–	58	37	30
	6793.26	4.07	−2.47	–	–	–	–
	6750.15	2.42	−2.62	91	–	–	–
	6752.71	4.64	−1.20	28	–	–	–
	6804.00	4.65	−1.67	–	–	–	26
	6810.26	4.61	−0.99	25	76	65	63
	6820.37	4.64	−1.17	27	–	–	–
	6858.15	4.61	−0.93	35	–	80	–
Fe II	4993.35	2.81	−3.67	46	65	–	–
	5234.62	3.22	−2.24	87	94	85	82
	5284.10	2.89	−3.01	66	87	72	–
	5325.56	3.22	−3.17	38	–	–	–
	5425.25	3.20	−3.21	48	–	–	–
	5534.83	3.25	−2.77	54	–	–	–
	5991.37	3.15	−3.56	28	–	–	–
	6084.10	3.20	−3.80	18	–	–	–
	6149.25	3.89	−2.72	30	–	–	41
	6247.55	3.89	−2.34	42	51	51	45
	6416.92	3.89	−2.68	30	46	50	38
	6432.68	2.89	−3.58	37	59	53	46

Table A2. Equivalent width measurements of other atomic lines considered in this study.

Element	Wavelength (Å)	χ (eV)	log gf	Ref	Equivalent widths (mÅ)			
					BD+03°2688	HE 0457−1805	HE 1255−2324	HE 2207−1746
Na I	5682.65	2.10	−0.70	PS	37	–	126	105
	5688.22	2.10	−0.40	PS	61	169	145	133
	6154.22	2.10	−1.57	R03	12	103	42	47
	6160.75	2.10	−1.27	R03	15	110	106	–
Mg I	4730.04	4.34	−2.39	R03	–	–	–	–
	5711.10	4.34	−1.68	R99	–	132	123	121
	6319.24	5.11	−2.16	Ca2007	–	–	43	42
	6319.49	5.11	−2.67	Ca2007	11	–	26	–
	8712.69	5.93	−1.26	Ca2007	–	–	–	–
	8717.83	5.91	−0.97	WSM	–	–	–	72
	8736.04	5.94	−0.34	WSM	65	120	129	117
Al I	6696.03	3.14	−1.481	MR94	–	67	62	54
	7835.32	4.04	−0.580	R03	–	76	57	42
	7836.13	4.02	−0.400	R03	–	–	–	52
	8772.88	4.02	−0.250	R03	–	82	90	–
	8773.91	4.02	−0.070	R03	–	110	102	–
Si I	5793.08	4.93	−2.06	R03	29	–	–	–
	6131.58	5.62	−1.69	E93	–	47	–	–
	6145.08	5.62	−1.43	E93	20	41	39	32
	6155.14	5.62	−0.77	E93	43	97	–	83
	8728.01	6.18	−0.36	E93	–	77	63	73
	8742.45	5.87	−0.51	E93	67	–	77	76
Ca I	5601.29	2.52	−0.52	C2003	–	147	–	–
	5857.46	2.93	+0.11	C2003	112	155	–	141
	5867.57	2.93	−1.61	C2003	15	–	40	31
	6102.73	1.88	−0.79	D2002	122	–	–	–
	6166.44	2.52	−1.14	R03	70	–	93	86
	6169.04	2.52	−0.80	R03	88	127	107	116
	6169.56	2.53	−0.48	DS91	105	148	129	126
	6449.82	2.52	−0.50	C2003	–	160	–	–
	6455.60	2.51	−1.29	R03	61	–	–	–
	6471.66	2.51	−0.69	S86	101	–	–	–
	6493.79	2.52	−0.11	DS91	127	–	156	144
	6499.65	2.52	−0.81	C2003	88	130	–	–
	6717.69	2.71	−0.52	C2003	101	–	–	–
Ti I	4512.74	0.84	−0.48	NIST	–	–	114	–
	4534.78	0.84	+0.28	NIST	–	–	–	139
	4617.28	1.75	+0.39	NIST	–	119	112	–
	4562.64	0.02	−2.66	NIST	–	–	–	69
	4758.12	2.25	+0.43	NIST	56	–	–	–
	4778.26	2.24	−0.33	NIST	–	–	45	44
	4997.10	0.00	−2.12	NIST	76	–	–	102
	5009.66	0.02	−2.26	NIST	63	–	–	–
	5016.17	0.85	−0.57	NIST	95	–	–	112
	5022.87	0.83	−0.43	NIST	99	137	–	–
	5039.96	0.02	−1.13	NIST	–	152	137	136
	5062.10	2.16	−0.46	NIST	21	67	47	–
	5087.06	1.43	−0.84	E93	46	–	–	–
	5113.45	1.44	−0.88	E93	30	82	–	–
	5147.48	0.00	−2.01	NIST	88	121	–	–
	5152.19	0.02	−2.02	NIST	72	–	93	99
	5210.39	0.05	−0.88	NIST	–	–	–	151
	5219.71	0.02	−2.29	NIST	74	–	–	–
	5223.63	2.09	−0.56	NIST	–	–	–	46
	5295.78	1.05	−1.63	NIST	24	72	52	51
	5490.16	1.46	−0.94	NIST	36	84	65	63
	5503.90	2.58	−0.19	NIST	–	46	–	–
	5662.16	2.32	−0.11	NIST	27	69	63	51
	5866.46	1.07	−0.87	E93	74	–	–	–
	5922.12	1.05	−1.47	NIST	31	–	–	61
	5978.55	1.87	−0.50	NIST	41	–	–	–
	6091.18	2.27	−0.37	R03	–	–	50	54

Table A2 – *continued*

Element	Wavelength (Å)	χ (eV)	log *gf*	Ref	Equivalent widths (mÅ) BD+03°2688	HE 0457−1805	HE 1255−2324	HE 2207−1746
	6258.11	1.44	−0.36	NIST	67	117	–	–
	6261.10	1.43	−0.48	NIST	67	–	–	108
	6554.24	1.44	−1.22	NIST	32	–	–	–
Cr I	4964.93	0.94	−2.53	NIST	48	–	–	74
	5193.50	3.42	−0.90	NIST	–	–	31	–
	5214.13	3.37	−0.74	NIST	–	–	32	–
	5214.61	3.32	−0.66	NIST	–	46	–	35
	5238.96	2.71	−1.30	NIST	–	–	38	–
	5247.57	0.96	−1.63	NIST	90	–	–	112
	5296.70	0.98	−1.39	GS88	103	–	–	–
	5298.28	0.98	−1.17	NIST	114	164	149	–
	5300.75	0.98	−2.13	R03	63	121	–	89
	5318.77	3.44	−0.69	NIST	–	–	41	–
	5 304.18	3.46	−0.71	NIST	–	–	–	15
	5 318.77	3.44	−0.69	NIST	–	38	–	–
	5 348.33	1.00	−1.29	NIST	106	159	134	–
	5 628.65	3.42	−0.77	NIST	–	35	25	–
	5 783.07	3.32	−0.29	NIST	14	–	–	39
	5 784.97	3.32	−0.38	NIST	16	72	63	49
	5 785.73	3.32	−0.51	NIST	–	–	–	48
	5 787.93	3.32	−0.08	R03	37	–	–	75
	6 330.10	0.94	−2.92	R03	49	–	–	–
Ni I	4 513.00	3.71	−1.52	NIST	–	–	36	–
	4 740.17	3.48	−1.78	NIST	–	47	–	–
	4 904.42	3.54	−0.19	NIST	71	–	108	–
	4 913.98	3.74	−0.60	NIST	33	–	–	–
	4 935.83	3.94	−0.34	NIST	46	–	–	69
	4 967.52	3.80	−1.60	NIST	–	37	–	–
	4 995.66	3.63	−1.61	NIST	–	53	–	25
	5 003.75	1.68	−3.13	NIST	–	82	–	–
	5 010.94	3.63	−0.90	NIST	–	–	71	–
	5 048.85	3.85	−0.37	NIST	45	–	–	–
	5 084.11	3.68	−0.18	E93	64	–	–	–
	5 115.40	3.83	−0.28	R03	52	–	92	–
	5 197.17	3.90	−1.14	NIST	–	62	–	–
	5 589.37	3.90	−1.15	NIST	–	–	–	33
	5 643.09	4.17	−1.25	NIST	–	–	35	–
	5 709.56	1.68	−2.14	NIST	89	130	–	–
	5 748.36	1.68	−3.25	NIST	37	96	79	–
	5 760.84	4.11	−0.81	NIST	23	71	–	–
	5 805.23	4.17	−0.60	NIST	13	–	–	45
	5 847.01	1.68	−3.44	NIST	–	86	69	54
	5 996.74	4.24	−1.06	NIST	–	36	–	23
	6 086.29	4.27	−0.47	NIST	21	–	–	–
	6 108.12	1.68	−2.49	NIST	73	–	–	104
	6 111.08	4.09	−0.83	NIST	–	70	–	–
	6 128.98	1.68	−3.39	NIST	27	–	67	–
	6 130.14	4.27	−0.98	NIST	–	–	–	22
	6 176.82	4.09	−0.26	R03	41	–	–	–
	6 177.25	1.83	−3.60	NIST	21	71	–	–
	6 186.72	4.11	−0.90	NIST	–	–	50	–
	6 230.10	4.11	−1.20	NIST	–	40	–	–
	6 322.17	4.15	−1.21	NIST	–	–	29	20
	6 327.60	1.68	−3.09	NIST	57	–	–	–
	6 378.26	4.15	−0.82	NIST	–	66	–	–
	6 384.67	4.15	−1.00	NIST	–	45	–	–
	6 482.80	1.94	−2.85	NIST	46	–	–	–
	6 532.88	1.94	−3.42	NIST	17	59	–	–
	6 586.33	1.95	−2.79	NIST	43	104	88	76
	6 598.61	4.24	−0.93	NIST	–	–	–	26
	6 635.14	4.42	−0.75	NIST	–	51	–	–
	6 767.77	1.83	−2.11	NIST	91	–	130	115

Table A2 – *continued*

Element	Wavelength (Å)	χ (eV)	log gf	Ref	Equivalent widths (mÅ) BD+03°2688	HE 0457−1805	HE 1255−2324	HE 2207−1746
	6 772.32	3.66	−0.97	R03	29	79	–	58
	6 842.04	3.66	−1.44	NIST	17	68	50	–
Sr I	4 607.33	0.00	+0.28	SN96	70	153	148	113
	4 872.49	1.80	−0.07	NIST	18	–	58	–
	7 070.07	1.85	−0.02	K2018	22	48	62	32
Y II	4 883.68	1.08	+0.07	SN96	132	–	–	–
	5 087.43	1.08	−0.17	SN96	115	–	167	–
	5 200.41	0.99	−0.57	SN96	100	141	133	122
	5 205.72	1.03	−0.34	SN96	105	145	–	123
	5 289.81	1.03	−1.85	R04	38	–	87	68
	5 402.78	1.84	−0.44	R03	54	91	99	79
Zr I	4 772.30	0.62	−0.06	A04	–	–	89	–
	4 784.94	0.69	−0.60	A04	–	64	67	46
	4 805.87	0.69	−0.58	A04	–	76	73	51
	4 809.47	1.58	0.35	A04	–	54	66	–
	4 815.05	0.65	−0.38	A04	–	–	–	46
	4 815.63	0.60	−0.27	A04	–	–	–	–
	4 828.05	0.62	−0.75	A04	–	57	69	35
	5 046.55	1.53	−0.18	A04	–	36	50	–
	5 385.13	0.52	−0.64	A04	–	76	–	51
	5 437.77	0.15	−2.12	A04	–	18	–	–
	5 620.13	0.52	−1.09	A04	–	45	–	33
	5 680.91	0.54	−0.86	A04	–	–	–	–
	5 879.79	0.15	−1.03	A04	–	83	89	53
	5 885.62	0.07	−1.73	A04	–	44	–	20
	5 955.34	0.00	−1.70	A04	–	53	–	31
	6 032.60	1.48	−0.35	A04	–	37	36	19
	6 127.46	0.15	−1.06	A04	–	99	83	64
	6 134.57	0.00	−1.28	A04	–	103	92	67
	6 140.46	0.52	−1.41	S96	16	–	–	–
	6 143.18	0.07	−1.10	S96	19	–	–	–
Mo I	5 238.20	3.21	+0.14	VALD	–	17	–	–
	5 360.51	3.24	+0.00	VALD	–	15	–	–
	5 506.49	1.33	+0.06	V2015	–	101	–	–
	5 533.03	1.33	−0.07	V2015	–	–	120	–
	5 858.27	1.47	−0.99	VALD	–	–	72	–
	6 030.63	1.53	−0.45	V2015	–	90	94	–
Ru I	4 869.15	0.93	−0.83	VALD	–	63	49	36
	5 309.27	0.93	−1.39	VALD	–	26	26	13
	5 636.24	1.06	−1.07	VALD	–	46	34	15
La II	5 303.53	0.32	−1.35	L01	77	114	107	99
	5 805.77	0.13	−1.56	L01	81	111	92	99
	6 262.29	0.40	−1.22	L01	185	–	–	–
	6 320.43	0.17	−1.52	SN96	110	183	162	145
	6 774.33	0.13	−1.71	VWR	117	193	185	166
Ce II	4 418.79	0.86	+0.27	L09	106	118	–	–
	4 486.91	0.29	−0.18	L09	108	–	100	96
	4 539.74	0.33	−0.08	L09	–	131	110	107
	4 562.37	0.48	+0.21	L09	122	139	120	122
	5 187.45	1.21	+0.17	L09	81	105	100	86
	5 274.24	1.04	+0.13	L09	86	106	93	90
	5 330.58	0.87	−0.40	L09	73	93	88	72
	5 393.39	1.10	−0.06	L09	–	107	–	–
	5 975.82	1.33	−0.45	L09	41	65	62	58
	6 043.37	1.21	−0.48	L09	50	–	–	71
Nd II	4 709.72	0.18	−0.97	DH	–	–	105	–
	4 763.62	0.38	−1.27	DH	59	84	86	77
	4 786.11	0.18	−1.42	DH	–	–	76	–
	4 797.15	0.56	−0.69	DH	–	100	92	–
	4 825.48	0.18	−0.42	DH	–	139	121	119
	4 859.03	0.32	−0.44	DH	108	–	–	124

Table A2 – *continued*

Element	Wavelength (Å)	χ (eV)	log *gf*	Ref	Equivalent widths (mÅ) BD+03°2688	HE 0457−1805	HE 1255−2324	HE 2207−1746
	4 902.04	0.06	−1.34	DH	–	107	93	97
	4 914.38	0.38	−0.70	DH	93	–	114	110
	5 063.72	0.98	−0.62	DH	76	80	91	77
	5 092.80	0.38	−0.61	DH	97	116	101	99
	5 192.61	1.14	−0.27	DH	90	–	101	100
	5 212.36	0.20	−0.96	DH	92	–	104	112
	5 234.19	0.55	−0.51	DH	–	115	112	99
	5 249.58	0.98	0.20	DH	98	122	–	104
	5 255.51	0.20	−0.67	DH	104	–	114	–
	5 293.16	0.82	0.10	DH	–	134	118	109
	5 306.46	0.86	−0.97	DH	51	74	71	75
	5 311.46	0.98	−0.42	DH	76	–	–	96
	5 319.81	0.55	−0.14	DH	106	133	119	114
	5 356.97	1.26	−0.28	DH	70	92	85	–
	5 371.93	1.41	−0.00	DH	79	–	–	–
	5 485.70	1.26	−0.12	DH	–	–	80	–
	5 698.92	1.54	−0.67	DH	–	–	–	–
	5 740.88	1.16	−0.53	DH	56	82	78	78
	5 811.57	0.86	−0.86	DH	58	85	81	73
Sm II	4 467.34	0.66	+0.15	L06	77	99	89	81
	4 499.48	0.25	−0.87	L06	70	77	–	61
	4 523.91	0.43	−0.39	L06	–	89	–	89
	4 566.20	0.33	−0.59	L06	68	89	82	–
	4 577.69	0.25	−0.65	L06	73	–	–	–
	4 676.90	0.04	−0.87	L06	88	88	89	–
	4 704.40	0.00	−0.86	L06	92	–	–	–
	4 791.60	0.10	−1.44	L06	47	–	66	57
Er II	4 675.62	1.32	−0.05	DeS	–	81	–	–
	4 759.65	0.00	−1.90	VALD	–	68	–	58
	4 831.15	1.62	−0.62	DeS	–	–	80	–
	4 872.09	1.61	−0.39	VALD	–	–	82	–
	4 879.89	1.62	−1.15	DeS	–	–	48	–
	6 006.78	0.00	−2.82	VALD	–	60	58	–

Note. *References:* (A04) Antipova et al. (2004); (C2003) Chen et al. (2003); (Ca2007) Carretta, Bragaglia & Gratton (2007); (D2002) Depagne et al. (2002); (DeS) De Smedt et al. (2016); (DH) Den Hartog et al. (2003); (DS91) Drake & Smith (1991); (E93) Edvardsson et al. (1993); (K2018) Karinkuzhi et al. (2018); (GS88) Gratton & Sneden (1988); (L01) Lawler, Bonvallet & Sneden (2001a); (L06) Lawler et al. (2006); (L09) Lawler et al. (2009); (MR94) McWilliam & Rich (1994); (NIST) Kramida et al. (2021); (PS) Preston & Sneden (2001); (R03) Reddy et al. (2003); (R04) Reyniers et al. (2004); (R99) Reddy, Bakker & Hrivnak (1999); (S86) Smith, Edvardsson & Frisk (1986); (S96) Smith et al. (1996); (SN96) Sneden et al. (1996); (VALD) Ryabchikova et al. (2015); (VWR) Van Winckel & Reyniers (2000); (V2015) Veklich, Lebid & Tmenova (2015); (WSM) Wiese, Smith & Miles (1969).

APPENDIX B: SUPPLEMENTARY FIGURES

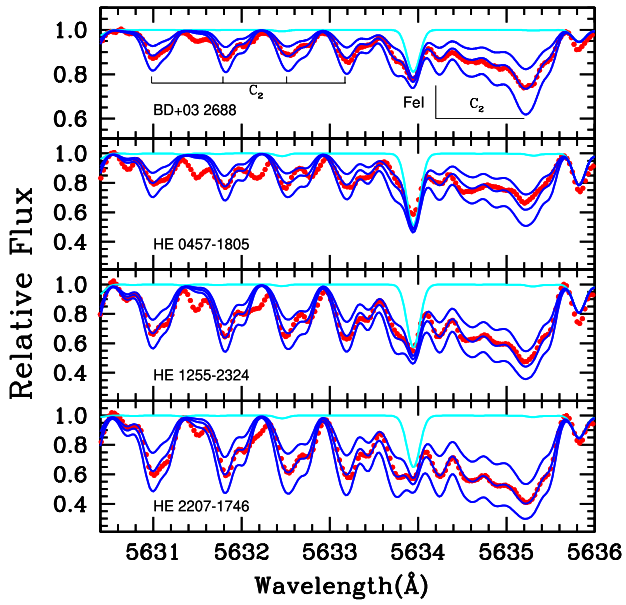

Figure B1. Observed (red dots) and synthetic (curves) spectra close to the region of the C_2 molecular band at 5 635 Å for the stars BD+03°2688, HE 0457−1805, HE 1255−2324, and HE 2207−1746. The upper cyan curves shown in the panels are synthetic spectra calculated without contribution from the C_2 lines. The middle blue curves are synthetic spectra calculated for the adopted solutions, $\log\epsilon(\mathrm{C}) = 7.67$, 8.36, 8.61, and 8.49 dex, that provide the best fits for BD+03°2688, HE 0457−1805, HE 1255−2324, and HE 2207−1746, respectively; the upper and lower blue curves show the spectral synthesis for $\Delta\log\epsilon(\mathrm{C}) = \pm 0.1$ dex around the adopted solutions.

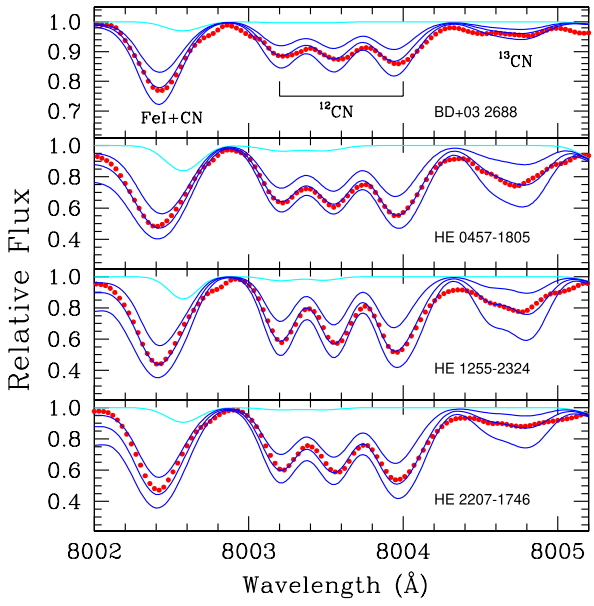

Figure B2. Observed (red dots) and synthetic (curves) spectra close to the region of the CN molecular band between 8 002 Å, and 8 005 Å for the stars BD+03°2688, HE 0457-1805, HE 1255-2324, and HE 2207-1746. The upper cyan curves shown in the panels are synthetic spectra calculated without contribution from the CN lines. The middle blue curves are synthetic spectra calculated for the adopted solutions, $\log\epsilon(\mathrm{N}) = 6.90$, 8.65, 8.44, and 8.27 dex, that provide the best fits for BD+03°2688, HE 0457-1805, HE 1255-2324, and HE 2207-1746, respectively; the upper and lower blue curves show the spectral synthesis for $\Delta\log\epsilon(\mathrm{N}) = \pm 0.3$ dex around the adopted solutions.

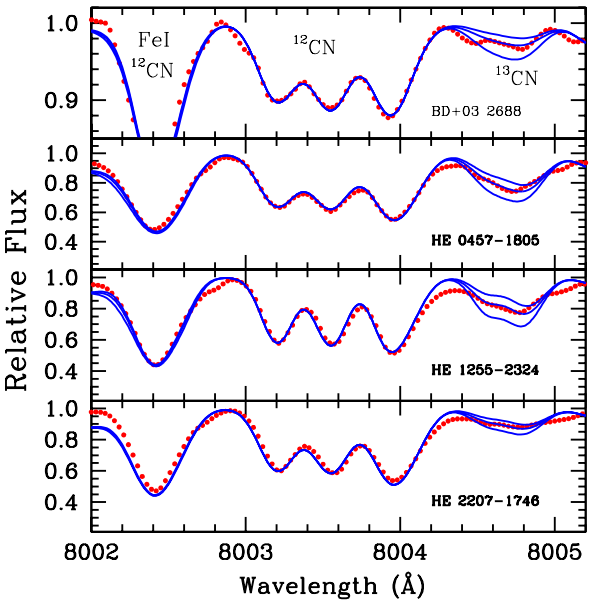

Figure B3. Observed (red dots) and synthetic (curves) spectra close to the region of the CN molecular band between 8 002 Å, and 8 005 Å for the stars BD+03°2688, HE 0457-1805, HE 1255-2324, and HE 2207-1746, calculated with different values for the $^{12}C/^{13}C$ isotopic ratios, considering the previous CNO abundances determined for these stars. For BD+03°2688, we show the synthesis for $^{12}C/^{13}C$ isotopic ratios of 10.0, 18.0 (adopted), and 30.0; for HE 0457-1805, the values are 30.0, 20.0 (adopted), and 10.0; for HE 1255-2324, the values are 30.0, 18.0 (adopted), and 10.0; for HE 2207-1746, the values are 20.0, 40.0 (adopted), and 90.0. For BD+03°2688, we enlarge the scale in order to better see the different values of $^{12}C/^{13}C$ isotopic ratio, since it is a lower metallicity object.

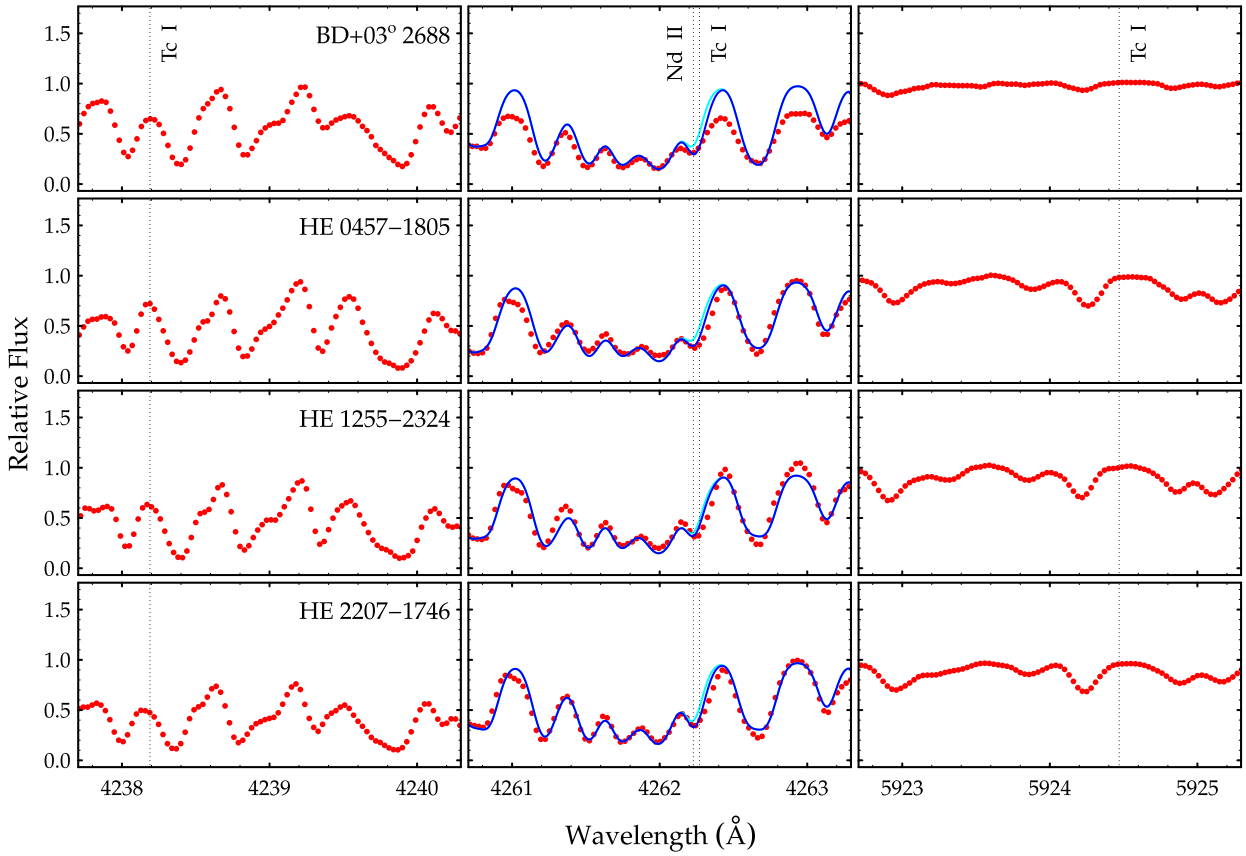

Figure B4. Observed (red dots) spectra close to the region of the Tc I lines at 4 238.19 Å, 4 262.27 Å, and 5 924.47 Å (dashed black lines) for the stars BD+03°2688, HE 0457-1805, HE 1255-2324, and HE 2207-1746. The spectral feature at 4 262.27 Å is strongly affected by the Nd II line at 4 262.23 Å, also identified on the middle panels. We then performed spectral synthesis for this region without contribution from the technetium line (cyan curves) and for $\log \epsilon(\mathrm{Tc}) = 1.0$ dex (blue curves).

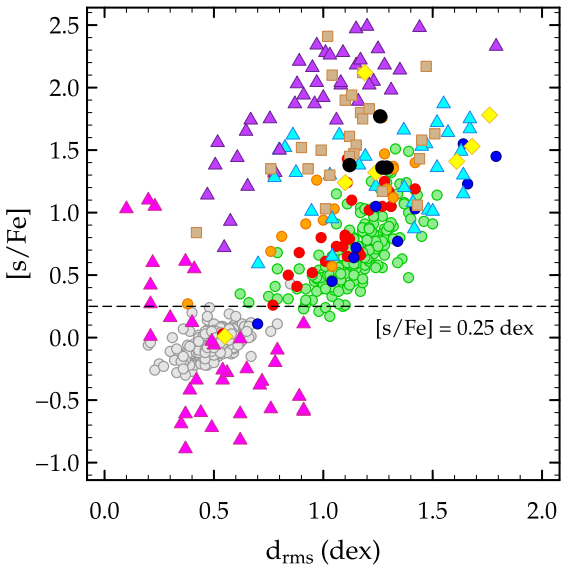

Figure B5. Diagram showing the [*s*/Fe] index against the d_{rms} distance for the program stars (black dots). Symbols have the same meaning as in Figs 12 and 13. Data for field giant stars (grey dots) were taken from the samples of Luck & Heiter (2007) and Mishenina et al. (2007). The dashed line in this figure represents the lower limit assumed by de Castro et al. (2016) for classify an object as a barium star.

APPENDIX C: ABUNDANCE UNCERTAINTIES

Table C1. Abundance uncertainties for BD+03°2688. Second column gives σ_{ran}, when three or more lines are used in the abundance derivation. Columns from 3 to 7 give the variation of the abundances caused by changes in T_{eff}, $\log g$, ξ, [Fe/H], and equivalent width measurements (W_λ), respectively. The eight column gives the composed uncertainties, by quadratically combining the terms from the third to seventh columns. The last column gives the abundance dispersion observed among the lines for those elements with three or more lines available.

Species	σ_{ran}	ΔT_{eff} +40 K	$\Delta\log g$ +0.3	$\Delta\xi$ +0.2 km s^{-1}	Δ[Fe/H] −0.1	ΔW_λ +3 mÅ	$\sqrt{\sum\sigma^2}$	σ_{obs} (n)
Na I	0.05	+0.04	−0.02	−0.01	+0.02	+0.08	0.11	0.09 (04)
Mg I	–	+0.02	−0.01	−0.04	+0.01	+0.08	0.09	–
Si I	0.07	+0.01	+0.04	−0.01	0.00	+0.07	0.11	0.13 (04)
Ca I	0.03	+0.06	−0.02	−0.08	+0.03	+0.07	0.13	0.10 (11)
Ti I	0.02	+0.08	−0.01	−0.04	+0.03	+0.07	0.12	0.10 (20)
Fe I	0.02	+0.05	−0.01	−0.09	+0.01	+0.06	0.12	0.13 (65)
Fe II	0.03	−0.02	+0.14	−0.04	−0.02	+0.07	0.17	0.09 (12)
Cr I	0.04	+0.07	−0.01	−0.07	+0.03	+0.07	0.13	0.14 (10)
Ni I	0.02	+0.05	+0.02	−0.04	+0.01	+0.07	0.10	0.11 (22)
Sr I	0.12	+0.06	−0.02	−0.07	+0.02	+0.08	0.17	0.21 (03)
Y II	0.07	+0.01	+0.10	−0.14	−0.02	+0.07	0.20	0.17 (06)
Zr I	–	+0.09	−0.01	−0.02	−0.01	+0.08	0.12	–
La II	0.04	+0.01	−0.12	−0.05	−0.03	+0.04	0.14	0.10 (05)
Ce II	0.08	+0.02	+0.11	−0.15	−0.02	+0.09	0.22	0.22 (08)
Nd II	0.04	+0.02	+0.12	−0.15	−0.01	+0.10	0.22	0.14 (16)
Sm II	0.08	+0.03	+0.11	−0.15	−0.01	+0.09	0.22	0.21 (07)
Eu II	–	−0.02	+0.09	0.00	−0.05	–	0.10	–
Pb I	–	+0.10	−0.20	0.00	0.00	–	0.22	–

Table C2. Abundance uncertainties for carbon, nitrogen, and oxygen, for the star BD+03°2688.

Species	ΔT_{eff} +40 K	$\Delta\log g$ +0.3	$\Delta\xi$ +0.2 km s^{-1}	$\Delta\log$ (C) +0.20	$\Delta\log$ (N) +0.20	$\Delta\log$ (O) +0.20	σ_{tot}
C	+0.02	+0.01	0.00	–	0.00	+0.07	0.07
N	+0.10	0.00	0.00	−0.27	–	+0.14	0.32
O	+0.02	+0.13	0.00	0.00	0.00	–	0.13

Table C3. Same as in Table C1, for the star HE 1255-2324.

Species	$\sigma_{\rm ran}$	$\Delta T_{\rm eff}$ +110 K	$\Delta\log g$ +0.3	$\Delta\xi$ +0.2 km s^{-1}	Δ[Fe/H] −0.1	ΔW_λ +3 mÅ	$\sqrt{\sum\sigma^2}$	$\sigma_{\rm obs}$ (n)
Na I	0.11	+0.09	−0.04	−0.06	+0.01	+0.04	0.16	0.21 (04)
Mg I	0.05	+0.06	0.00	−0.03	0.00	+0.05	0.11	0.10 (04)
Al I	0.01	+0.05	−0.02	−0.04	0.00	+0.04	0.08	0.02 (04)
Si I	0.04	−0.03	+0.07	−0.03	−0.02	+0.05	0.11	0.07 (03)
Ca I	0.02	+0.11	−0.04	−0.08	+0.01	+0.05	0.15	0.05 (05)
Ti I	0.02	+0.15	−0.02	−0.08	+0.01	+0.06	0.18	0.07 (10)
Fe I	0.03	+0.09	+0.03	−0.08	0.00	+0.06	0.14	0.16 (31)
Fe II	0.07	−0.08	+0.18	−0.07	−0.04	+0.06	0.23	0.15 (05)
Cr I	0.04	+0.10	−0.02	−0.05	+0.01	+0.06	0.13	0.12 (08)
Ni I	0.02	+0.06	+0.05	−0.07	−0.01	+0.06	0.12	0.07 (13)
Rb I	–	+0.10	0.00	−0.10	0.00	–	0.14	–
Sr I	0.14	+0.13	−0.04	−0.08	+0.01	+0.06	0.22	0.24 (03)
Y II	0.07	+0.01	+0.09	−0.15	−0.04	+0.05	0.20	0.14 (04)
Zr I	0.03	+0.18	−0.01	−0.09	+0.02	+0.07	0.22	0.10 (10)
Nb I	0.09	+0.20	0.00	−0.05	0.00	–	0.22	0.15 (03)
Mo I	0.01	+0.17	−0.01	−0.14	+0.01	+0.06	0.23	0.02 (03)
Ru I	0.02	+0.15	0.00	−0.03	0.00	+0.06	0.17	0.03 (03)
La II	0.06	+0.04	−0.15	−0.09	−0.03	+0.05	0.20	0.12 (04)
Ce II	0.06	+0.03	+0.11	−0.17	−0.04	+0.07	0.23	0.16 (07)
Nd II	0.03	+0.04	+0.12	−0.17	−0.03	+0.07	0.23	0.15 (20)
Sm II	0.06	+0.03	+0.12	−0.17	−0.04	+0.07	0.23	0.11 (04)
Eu II	–	+0.01	+0.15	−0.02	−0.03	–	0.15	–
Er II	0.08	+0.01	+0.13	+0.11	−0.03	+0.07	0.20	0.16 (04)
W I	–	+0.15	0.00	−0.10	0.00	–	0.18	–
Tl I	–	+0.15	+0.05	−0.05	0.00	–	0.17	–
Pb I	–	+0.40	+0.10	0.00	0.00	–	0.41	–

Table C4. Abundance uncertainties for carbon, nitrogen, and oxygen, for the star HE 1255-2324. The last line of this table provides the uncertainty estimate in the ^{12}C/^{13}C isotopic ratio.

Species	$\Delta T_{\rm eff}$ +110 K	$\Delta\log g$ +0.3	$\Delta\xi$ +0.2 km s^{-1}	$\Delta\log$ (C) +0.2	$\Delta\log$ (N) +0.2	$\Delta\log$ (O) +0.2	$\sigma_{\rm tot}$
C	+0.04	0.00	0.00	–	0.00	+0.08	0.09
N	+0.30	+0.06	0.00	−0.29	–	+0.30	0.52
O	+0.05	+0.16	0.00	−0.15	−0.10	–	0.25
^{12}C/^{13}C	+4.0	0.0	0.0	–	–	–	4.0

This paper has been typeset from a TEX/LATEX file prepared by the author.